Sensitisation of Austenitic Stainless Steels

By
Chia Hooi Too
Queens' College

University of Cambridge
Department of Materials Science and Metallurgy
Pembroke Street, Cambridge CB2 3QZ

A dissertation submitted for the
degree of Master of Philosophy
at the University of Cambridge
August 2002

Preface

This dissertation is submitted for the degree of Master of Philosophy in Modelling of Materials at the University of Cambridge. The research described herein was conducted under the supervision of Professor H. K. D. H. Bhadeshia and Dr T. Sourmail in the Department of Materials Science and Metallurgy, University of Cambridge, between May 2002 and August 2002.

This work is to the best of my knowledge original, except where acknowledgements and references are made to previous work. Neither this, nor any substantially similar dissertation has been or is being submitted for any other degree, diploma or other qualification at any other university. This dissertation contains less than 15,000 words.

Chia Hooi Too

August 2002

Acknowledgements

I would like to express my sincere thanks to Professor H. K. D. H. Bhadeshia for his constant support, encouragement, knowledge and friendship. I am extremely grateful to Dr T. Sourmail for his valuable guidance.

I am indebted to the Foreign and Commonwealth Office, London and the Cambridge Commonwealth Trust for financial support, the Cambridge–Malaysia Chevening Scholarship.

I would like to thank all the members of Phase Transformations and Complex Properties Research Group for their friendship and assistance. Thanks to all my friends for their support and friendship.

Finally, I would like to take this opportunity to express my gratitude to my family members for their love, unfailing encouragement and support, specially my parents. Special thanks to Don Ri for his endless love, care, encouragement and support.

Abstract

Austenitic stainless steels with excellent corrosion resistance and good weldability have wide applications in industry. These iron–based alloys contain a high level of chromium which forms a protective oxide film on the surface and hence resists corrosion. The oxide film regenerates when damaged, making the steel 'stainless'. However, carbide precipitation due to the welding process or heat treatment can cause the occurrence of chromium–depleted zones at the grain boundaries, leading to a phenomenon known as sensitisation, in which the depleted zones become the focus of intense corrosion.

Considerable research has been conducted in the past to model grain boundary precipitation in the context of sensitisation. Several previous attempts on carbide formation are discussed. Comparisons are made between these models based on thermodynamic and kinetic modelling. All the previous work on modelling grain boundary precipitation has treated multicomponent systems with a pseudo–binary approximation. However, in practice, there are significant multicomponent effects which determine the course of precipitation.

The present work is concerned with the development of a physical model taking into account the multicomponent effects to predict the likelihood of sensitisation in austenitic stainless steels. By interfacing with thermodynamic software, complex equilibrium calculations can be performed with the resulting physical model, avoiding unnecessary approximations made in previous work. A numerical approach is applied to estimate the concentration profile of all elements in the vicinity of grain boundaries based on free energy gradients rather than concentration gradients. The numerical method has the further major advantage that changing boundary conditions can be readily accomodated.

As the effects of complex multicomponent system are properly accounted for in the present model, the calculations obtained are found to be in good agreement with published literature data. It is further proved that the model can accurately predict the diffusion profiles for all elements in the vicinity of the grain boundary.

Future work can be conducted to include the effects of grain boundary diffusion on modelling the kinetics of precipitation reactions. The grain boundary structure size may also be important variables.

Contents

Nomenclature and Abbreviations

g	the grain size of austenite
r	the radius of the precipitate
t	the time
t_h	the time for self–healing process
t_s	the sensitisation time
t_d	the desensitisation time
R	the gas constant
T	the absolute temperature of the system
G_i^o	the free energy of the pure element i in the austenite phase relative to its reference state
G_γ	the free energy of the system in γ phase
$\Delta G^o_{\mathrm{M_{23}C_6}}$	the Gibbs free energy of formation of precipitate indicated in subscript
ΔG	the Gibbs free energy change
D_i^γ	the volume diffusion coefficient of element i in phase γ
D_{ij}^γ	the cross–diffusion coefficient of elements i and j
a_i	the activity of element i
$\bar{c}_i^\gamma$	the average concentration of element i in phase γ
c_i^γ	the concentration of element i in phase γ
$c_i^{\gamma\beta}$	the concentration of element i in phase γ in equilibrium with β
$c_{i(critical)}^{\gamma\beta}$	the critical concentration value of element i in phase γ in equilibrium with β that initiates sensitisation
$\bar{x}_i^\gamma$	the average mole fraction of element i in phase γ
x_i^γ	the mole fraction of element i in phase γ
$x_i^{\gamma\beta}$	the mole fraction of element i in phase γ in equilibrium with β
J_i	the flux of element i
M_i	the mobility of element i
μ_i	the chemical potential of element i
Q_i	the activation energy of element i
y_i	the site fraction occupancy of element i on its sublattice
V_m^γ	the molar volume of the phase γ
V_i^p	the partial molar volume for element i
W	the width of the depleted zone
MTDATA	Metallurgical and Thermochemical Databank
SGTE	Scientific Group Thermodata Europe
CALPHAD	CALculation of PHAse Diagram
TTC	Time–temperature–concentration
HAZ	Heat–affected zone
fcc	face–centered–cubic
f.o.r.	frame of reference

Chapter 1

Introduction

Austenitic stainless steels are used widely in many sectors such as the food, chemical, power, pharmaceutical, and building industries [1]. The high levels of chromium contribute to the excellent corrosion resistance in austenitic stainless steel, making it suitable for use in submarine nuclear plant. However, the presence of a chromium–depleted zone due to carbide precipitation in the vicinity of grain boundaries can sensitise the austenitic stainless steels, increasing the tendency for severe intergranular corrosion. The aim of the work presented in this chapter was to provide a brief background on austenitic stainless steels and the sensitisation process.

1.1 Austenitic Stainless Steels

Austenitic stainless steel is essentially an iron–chromium–nickel alloy, containing between 18 and 30 wt% chromium, 8–20 wt% nickel and 0.03–0.1 wt% carbon [2]. It retains the austenitic structure (Figure 1.1) to ambient temperature.

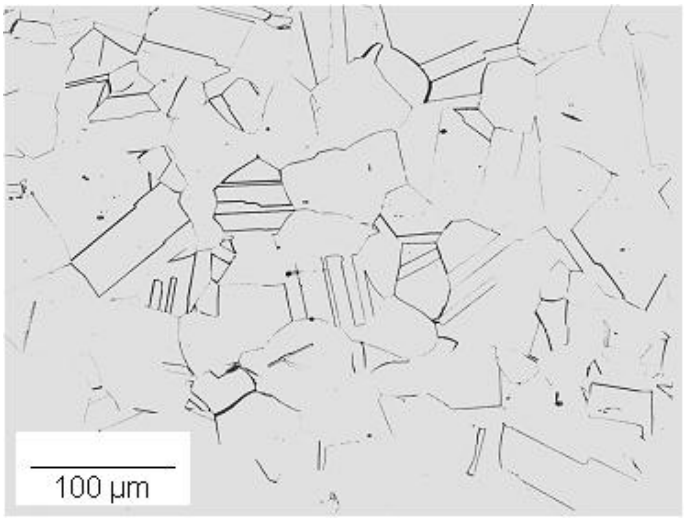

Figure 1.1: General microstructure of austenitic stainless steel [3].

Austenitic stainless steels are used in a wide range of applications due to their excellent corrosion resistance and good weldability. The corrosion resistance of the steel is enhanced by the addition of chromium to create a compact, continuous, insulating, coherent and regenerative protective chromium oxide film on the surface. Although the minimum chromium content for corrosion resistance is 10.5 wt%, most stainless steels contain 17–18 wt% of chromium as the passivity increases with concentration up to 17 wt% [3]. As chromium is a ferrite stabiliser, nickel is added to stabilise the austenitic structure at all temperatures. Other alloying elements such as molybdenum, titanium, manganese may be present to improve the mechanical properties of the steel. Typical compositions of the American Iron and Steel Institute (AISI) 300 series austenitic stainless steels are shown in Table 1.1.

	Composition / wt%						
AISI type	**Cr**	**Ni**	**C**	**Si**	**Mn**	**P**	**S**
302	17–19	8.0–10.0	0.15	1.0	2.0	0.045	0.03
303	17–19	8.0–10.0	0.15	1.0	2.0	0.2	0.15
304	18–20	8.0–12.0	0.08	1.0	2.0	0.045	0.03
304L	18–20	8.0–12.0	<0.03	1.0	2.0	0.045	0.03
310	24–26	19–22	0.25	1.5	2.0	0.045	0.03
314	23–26	19–22	0.25	1.5–3.0	2.0	0.045	0.03
316	16–18	10–14	0.08	1.0	2.0	0.045	0.03
316L	16–18	10–14	<0.03	1.0	2.0	0.045	0.03

Table 1.1: Typical compositions of austenitic stainless steels [4].

1.2 Sensitisation and Desensitisation

Sensitisation refers to the breakdown in corrosion resistance which may occur if austenitic stainless steels are cooled slowly from the solution anneal temperature (≈1100 °C) or are reheated in the temperature range from 550 °C to 850 °C. Sensitisation is associated with the precipitation of chromium–rich carbides such as $M_{23}C_6$ or M_7C_3 along grain boundaries during the detrimental heat treatments [5]. The 'M' represents metal atoms, mainly chromium. During carbide precipitation, interstitial carbon can diffuse rapidly to the grain boundaries. Unlike carbon, chromium diffuses much more slowly, resulting in the chromium–depleted zone at the grain boundaries as illustrated in Figure 1.2. The steel then becomes deficient in chromium at the grain boundary region and no longer resists corrosion. The steel is said to be in a sensitised state and is susceptible to intergranular corrosion. When the intergranular corrosion propagates along grain boundaries from the surface into the material, grain dropping may occur, leading to material mass–loss as shown in Figure 1.3.

In a welding process, when regions close to the weld in the heat–affected zone (HAZ) are heated within the sensitisation temperature range 550 °C to 850 °C,

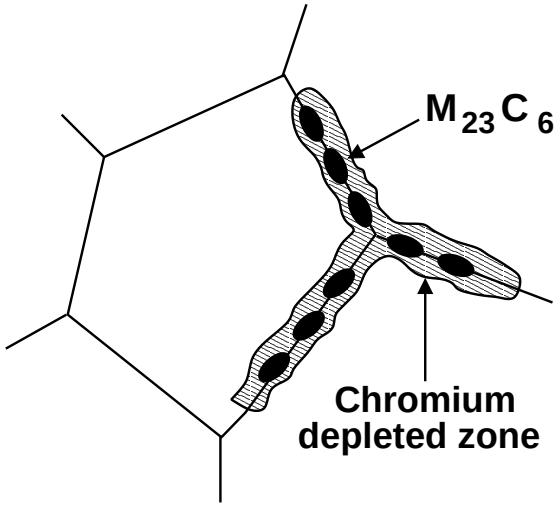

(a)

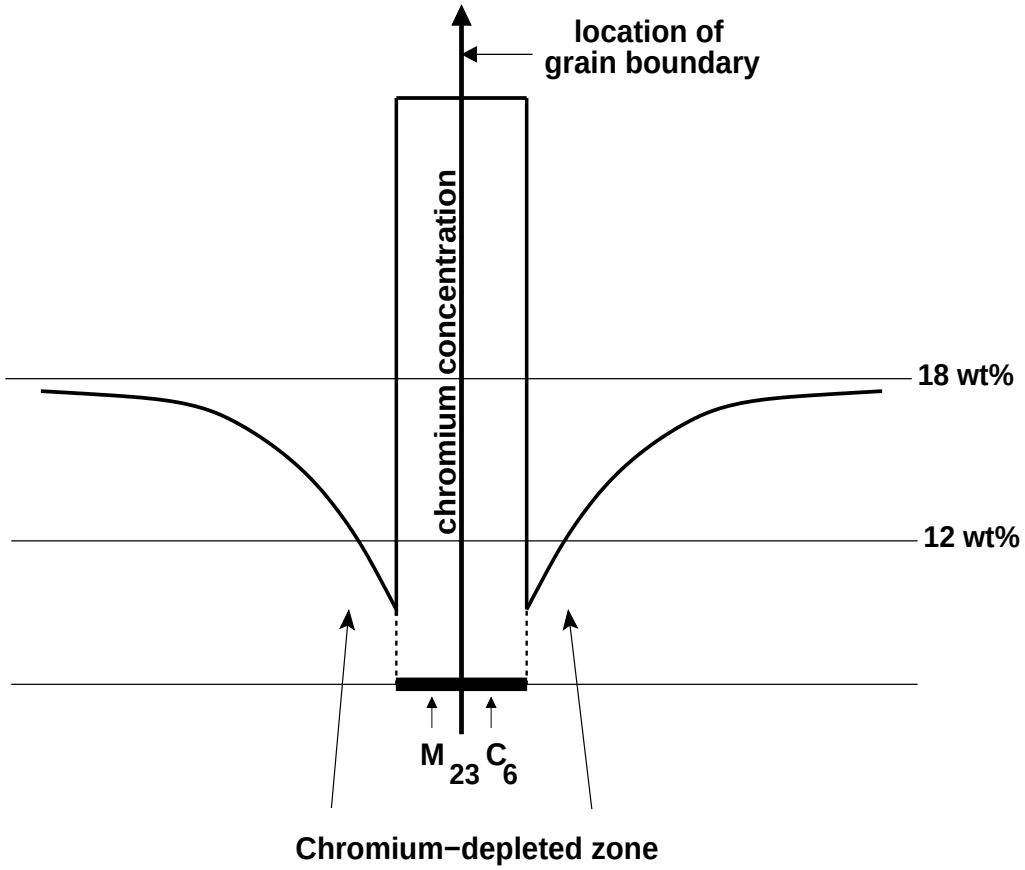

(b)

Figure 1.2: Schematic diagram showing the chromium–depleted zone at a grain boundary [1].

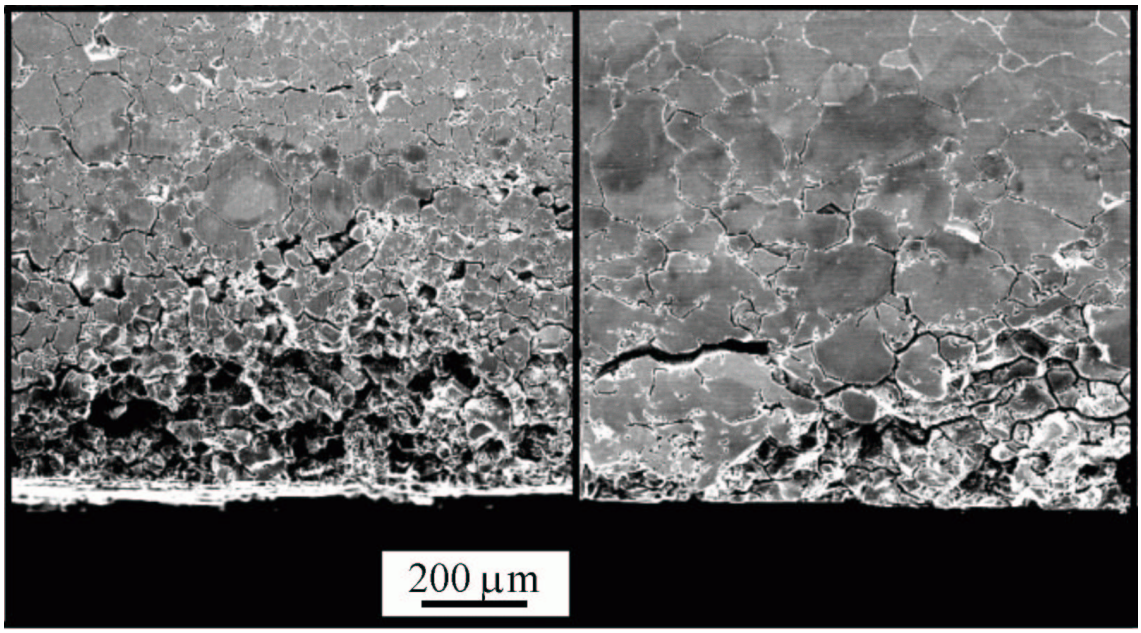

Figure 1.3: Micrographs showing grain dropping due to intergranular corrosion. After [6].

chromium–depletion will occur and the susceptibility to intergranular attack can arise. This type of corrosion due to sensitisation is known as 'weld decay' [7].

A self–healing process, also known as desensitisation, refers to the return of corrosion resistance of the stainless steels after prolonged heat treatment in the temperature range which initially causes sensitisation. Self–healing begins when the chromium content at the carbide–matrix interface increases due to the chromium diffusion from the matrix further away from the grain boundaries [8].

There are several ways to counteract the sensitisation of austenitic stainless steels. The chromium–depleted zone in the vicinity of grain boundaries can be homogenised by prolonged heat treatment which is the self–healing process described above. Alternatively, the addition of strong carbide formers such as titanium and niobium can prevent the formation of chromium–rich carbides and thus stabilise the steels. The minimisation of carbon content is another way to avoid sensitisation. Figure 1.4 shows two curves representing the temperature range that induce carbide precipitation in steels with 0.15 wt% C and 0.05 wt% C. It can be seen clearly that the time required to initiate sensitisation in lower carbon content (0.05 wt%) steel is greater [7]. Therefore, by minimising the carbon content in the steel, it is possible to avoid sensitisation.

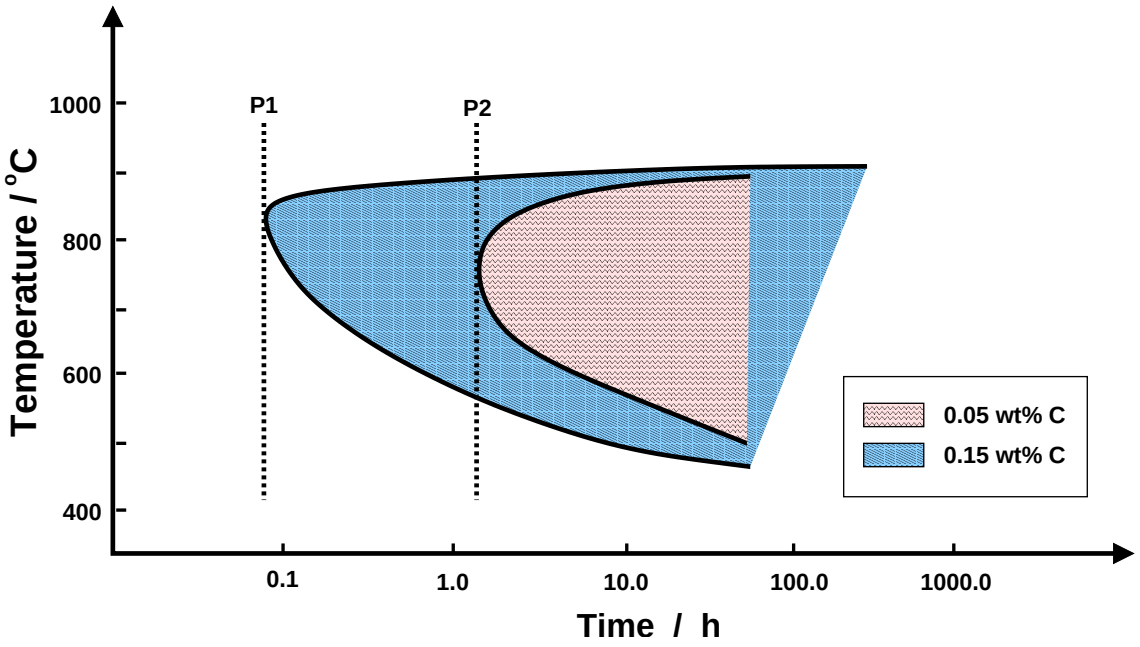

Figure 1.4: Effect of carbon content in steel on sensitisation conditions. Longer heat treatment time is required for low carbon steel to cause sensitisation (comparing P1 and P2). After [7].

Chapter 2

Thermodynamics and Kinetics of Sensitisation

Sensitisation–related research has been conducted extensively over the past 30 years. Physical modelling began with the proposal that the chromium–depletion zone is responsible for sensitisation [9]. During detrimental heat–treatments, chromium carbides precipitate along the grain boundaries. As the carbides grow, the chromium–depletion zone increases and sensitisation occurs.

Modelling of carbide formation and the development of the chromium–depletion zone involves thermodynamic and kinetic modelling. Selected previous attempts for the modelling grain boundary precipitation and predicting sensitisation are summarised in Table 2.1.

2.1 General Introduction

The growth rate of a precipitate forming in a metastable matrix can be diffusion–controlled, interface–controlled or mixed–controlled. When most of the free energy is dissipated in diffusion, the interface is said to be diffusion–controlled. On the other hand, the growth rate is interface–controlled when the majority of the free energy is dissipated in transferring atom across the interface. Figure 2.1 below illustrates the concentration profile at the interface of these rate–controlling processes.

2.2 Zener's Theory

Most of the previous work on growth kinetics has been based on Zener's theory (1949). The theory is for diffusion–controlled growth in binary systems. The two assumptions for this theory are: (a) the concentration gradient in the matrix is constant and (b) the far–field concentration $\bar{c}$ never changes.

In a binary system, the concentrations at the interface for an isothermal transformation can be obtained as shown in Figure 2.2.

Model	Year	Description	Reference
Stawström & Hillert	1969	A diffusion–controlled model was developed to model the process of grain boundary precipitation and the formation of chromium–depleted zone.	[8]
Hall & Briant	1984	Development of a simple model to determine chromium concentration at the grain boundary region.	[5]
Was & Kruger	1985	An integrated thermodynamic and kinetic model was developed to quantitatively model the chromium–depleted zone adjacent to a grain boundary in Ni–Cr–Fe alloys.	[10]
Bruemmer	1990	A theoretically based, empirically modified model was developed to quantitatively predict the degree of sensitisation.	[9]
Mayo	1997	A semi–empirical model of chromium diffusion was developed to predict the minimum chromium concentration at the grain boundary and estimate the depletion zone halfwidth for the thermal treatments.	[11]
Sahlaoui *et al.*	2002	A two–stage diffusional model to predict the evolution of chromium profiles resulting from carbide precipitation during aging.	[12]

Table 2.1: List of previous models on grain boundary precipitation.

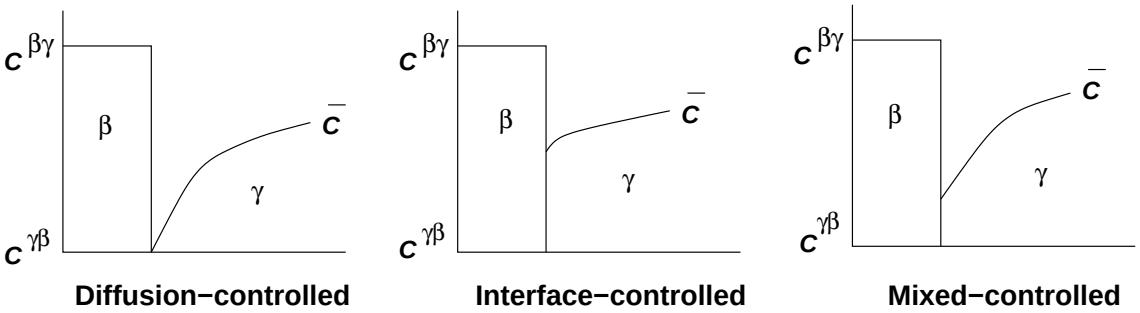

Figure 2.1: Schematic illustration of the concentration profile at the interface for different rate–controlling processes. $c^{\gamma\beta}$ is the concentration of solute of the matrix in equilibrium with β, $c^{\beta\gamma}$ is the concentration of precipitate in equilibrium with γ. $\bar{c}$ is the far–field concentration [13].

In this model, the flux of solute at the interface is equal to the rate at which the solute is absorbed:

$$\left(c^{\beta\gamma} - c^{\gamma\beta}\right) \frac{\partial z^*}{\partial t} = D^{\gamma} \frac{\partial c}{\partial z}\bigg|_{z=z^*} \approx D^{\gamma} \frac{\bar{c} - c^{\gamma\beta}}{\Delta z} \tag{2.1}$$

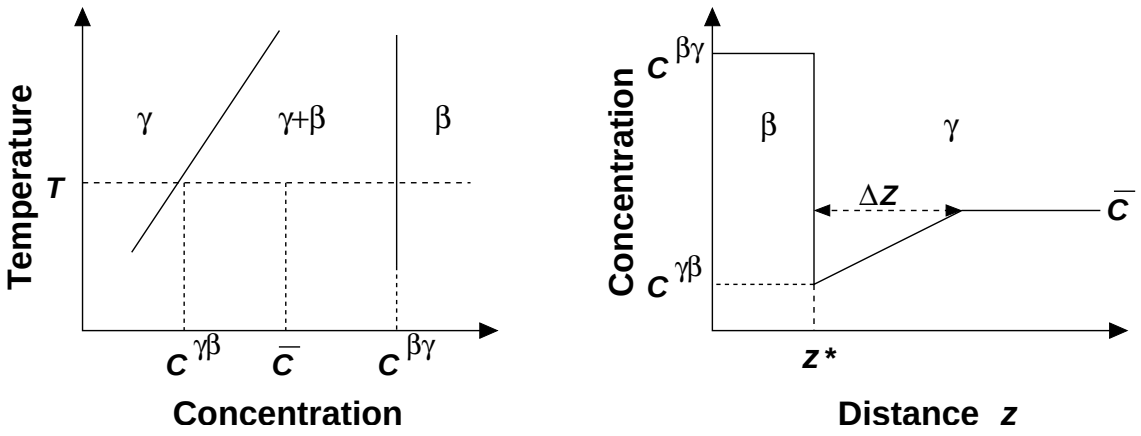

Figure 2.2: Phase diagram and the concentration profile at the diffusion–controlled growth interface [13].

where z^* is the position of the interface, D^γ is the volume diffusion coefficient, t is time and c is the concentration of solute. The conservation of solute implies:

$$\left(c^{\beta\gamma} - \bar{c}\right) z^* = \frac{1}{2}\left(\bar{c} - c^{\gamma\beta}\right) \Delta z \tag{2.2}$$

On combining all the equations:

$$\frac{\partial z^*}{\partial t} = \frac{D^\gamma \left(\bar{c} - c^{\beta\gamma}\right)^2}{2z^* \left(c^{\gamma\beta} - c^{\beta\gamma}\right)\left(c^{\gamma\beta} - \bar{c}\right)} \tag{2.3}$$

This leads to:

$$z^* \propto \sqrt{D^\gamma t} \tag{2.4}$$

This shows that the precipitate thickens with the square root of time, giving parabolic thickening during one–dimensional growth.

2.3 Earlier models

2.3.1 Thermodynamic Modelling

All the earlier models assumed that all of the carbon forms carbides at an early stage. When all the carbon has precipitated, the chromium content at the carbide–matrix interface is considered to be at its lowest point. On further annealing, the diffusion of chromium to the depleted zone will increase the chromium concentration at the carbide–matrix interface until self–healing is accomplished. In other words, self–healing begins only after the carbide precipitation has finished.

2.3.2 Kinetic Modelling

For kinetic modelling, most of the previous models assume that carbides precipitate at an early stage due to the high diffusivity of carbon. It is assumed that the chromium content at the carbide–matrix interface is rather low during precipitation, thus causing chromium diffusion from the adjacent zone of the matrix to the interface. When all the carbon has transformed into carbide, precipitation is considered as complete. On further annealing, the interface chromium content will increase and a self–healing process occurs. The width of the depleted–zone W is calculated based on random–walk theory [8] as:

$$\frac{1}{2}W \approx \sqrt{2D^{\gamma}t} \tag{2.5}$$

where D^{γ} is the diffusion coefficient and t is time. The chromium concentration in matrix (γ) in equilibrium with the precipitate phase (β) can be determined based on Zener's theory. The composition of carbide is approximated as $Fe_7Cr_{16}C_6$ so the chromium fraction in the carbide will thus be $\frac{16}{6}\bar{c}_C^{\gamma}$. With the assumption that all carbon will form carbides, the chromium content ($c_{Cr}^{\gamma\beta}$) can be calculated as:

$$\left(\bar{c}_{Cr}^{\gamma} - c_{Cr}^{\gamma\beta}\right)\sqrt{2D^{\gamma}t} = \frac{1}{2}g\left(\frac{16}{6}\bar{c}_C^{\gamma}\right) = 1.3g\bar{c}_C^{\gamma} \tag{2.6}$$

where g is the grain size of austenite. If the critical value of chromium concentration for sensitisation to occur is assumed as 13 wt%, the time for self–healing process is calculated as:

$$t_h \approx \frac{1}{D^{\gamma}}\left(\frac{g\bar{c}_C^{\gamma}}{\bar{c}_{Cr}^{\gamma} - 0.13}\right)^2 \tag{2.7}$$

2.4 Stawström and Hillert model

2.4.1 Thermodynamic Modelling

Stawström and Hillert (1969) [8] developed a model for grain boundary precipitation in 18Cr–8Ni–C (wt%) stainless steels. It was assumed that there is a local equilibrium between the carbide and austenite at the interface. As carbon diffuses orders of magnitude faster than chromium, it was assumed that the carbon activity in the whole material is almost even. This is referred to as carbon isoactivity.

In general, the tie–line satisfying the bulk mass balance (that going through the bulk composition in Figure 2.3) does not correspond to that verifying carbon isoactivity. To identify the isoactivity tie–line (that for which the chemical potential of carbon is identical in the bulk and at the interface), Stawström and Hillert used the unpublished data by Nishizawa [14]. The initial composition of the steel studied was

19.1 wt% Cr and 7.5 wt% Ni. The critical chromium concentration for sensitisation is assumed to be 13 wt% Cr and the interaction effect between nickel and chromium was neglected. Based on these few assumptions, the initial carbon activity was calculated as [8]:

$$RT\ln a_C = RT\ln \bar{c}_C^{\gamma} + 5443(\bar{c}_{Cr}^{\gamma})^2 - 113044\bar{c}_{Cr}^{\gamma} - 18.84T + 49220 \qquad (2.8)$$

where a_C is the carbon activity, $\bar{c}_C^{\gamma}$ and $\bar{c}_{Cr}^{\gamma}$ are the initial carbon and chromium concentrations in steel. By calculating the activity of carbon for a number of points on the $\gamma/\gamma+\beta$ boundary, it is possible to associate an 'isoactivity tie–line' to each bulk composition as illustrated in Figure 2.3. The chromium concentration at the carbide–matrix interface can thus be determined.

The carbon activity decreases as the precipitate forms, so the interface chromium content will gradually increase according to the tie–line as indicated by the arrow in Figure 2.3. This shows that precipitation continues even during self–healing.

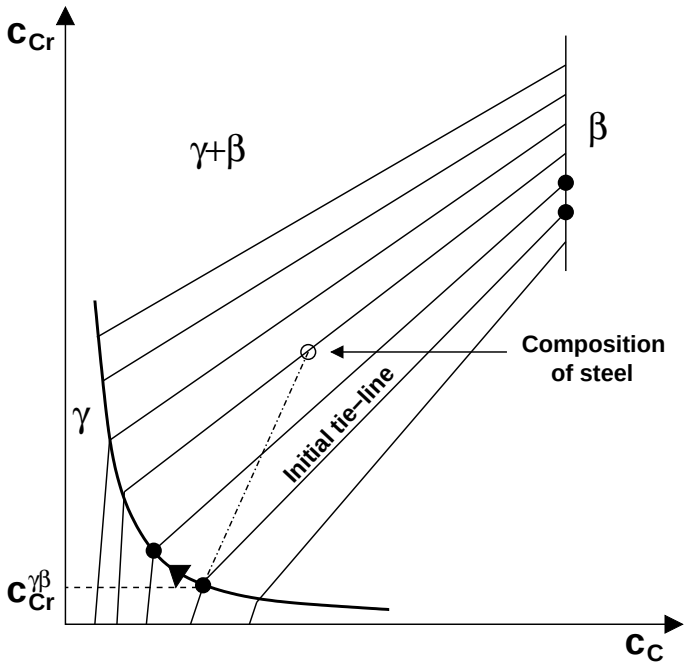

Figure 2.3: Schematic phase diagram showing the change of equilibrium during precipitation.

Stawström and Hillert's model takes into account the carbon activity in the calculation of the chromium content at the matrix–carbide interface. However, the interaction effect between nickel and chromium in the system is neglected. Furthermore, the calculation of the carbon activity in this model cannot be performed for more complex systems such as Fe, Cr, Ni, Mo, Mn, C..... nor for steels with significantly different levels of nickel content.

2.4.2 Kinetic Modelling

Stawström and Hillert established a diffusion–controlled model for the precipitation of carbides and the development of a chromium–depleted zone at the grain boundary region in stainless steels. It was shown that the whole precipitation process can be modelled using the same diffusional process rather than two different mechanisms.

Previously, Shvartz and Kristal [15] suggested carbon diffusion–controlled growth for sensitisation and chromium diffusion–controlled growth for self–healing. According to the depleted zone theory, the precipitation process rate is determined by the slow rate of chromium diffusion. Therefore, the activation energy of the process in which the steel is susceptible to sensitisation must equal the activation energy of the diffusion of chromium. However, based on Levin's calculation [16], it appeared that the calculated activation energy for sensitisation process corresponded to the values of carbon diffusion process and not of chromium. Thus, Shvartz and Kristal [15] suggested different mechanisms for sensitisation and self–healing processes.

Bäumel *et al.* [17] also introduced two different chromium mechanisms which were grain boundary diffusion for sensitisation and volume diffusion for desensitisation. In this model, Stawström and Hillert managed to prove Bendure *et al.*'s [18] observation that the carbide film will continue to grow at annealing times long enough to cause desensitisation. As the carbon content of the austenite decreases, the carbon activity of the steel will decrease and thus allow the chromium content in the depleted zone to increase.

A number of further assumptions are made in Stawström and Hillert's model. Firstly, it is assumed that an uniform thickness grain boundary film is formed and thus the diffusion in the matrix can be treated as one–dimensional. Secondly, as the diffusion coefficient of carbon is several orders of magnitude higher than chromium, it is assumed that there is an even carbon activity at all times in the whole material. It is also assumed that the diffusivity of chromium in the carbide is sufficiently high to keep the chromium content there at a constant level.

As the precipitation reaction is assumed mainly to be controlled by chromium diffusion in the austenite in this model, the basic rate equation is obtained based on Fick's 2^{nd} law and the mass balance theory as in Zener's model. By assuming the concentration gradient in the matrix is constant, the flux of chromium at the interface is given as:

$$J_{Cr} = D^{\gamma}_{Cr} \frac{\bar{x}^{\gamma}_{Cr} - x^{\gamma\beta}_{Cr}}{V^{\gamma}_{m} \Delta z} \tag{2.9}$$

where D^{γ}_{Cr} is the diffusion coefficient of chromium, $\bar{x}^{\gamma}_{Cr}$ is the initial mole fraction of chromium in the matrix, $x^{\gamma\beta}_{Cr}$ the chromium mole fraction in matrix in equilibrium with precipitates and V^{γ}_{m} is the molar volume of the matrix phase. It is assumed that the sum of the fluxes of Fe and Cr in Fe–Cr–C alloys is zero as they are of opposite directions.

$$J_{Cr} + J_{Fe} = 0 \tag{2.10}$$

Consider the transformation of a thin layer of austenite ∂b to a layer of carbide ∂z^*. The mass balance equations for chromium and iron are given as [8]:

$$\frac{\partial z^*}{\partial t}\frac{x_{Cr}^{\beta\gamma}}{V_m^\beta} - \frac{\partial b}{\partial t}\frac{x_{Cr}^{\gamma\beta}}{V_m^\gamma} = -J_{Cr} \tag{2.11}$$

$$\frac{\partial z^*}{\partial t}\frac{x_{Fe}^{\beta\gamma}}{V_m^\beta} - \frac{\partial b}{\partial t}\frac{x_{Fe}^{\gamma\beta}}{V_m^\gamma} = -J_{Fe} \tag{2.12}$$

where V_m^β is the molar volume of precipitate phase. On combining Equations 2.10, 2.11 and 2.12:

$$J_{Cr} = -\frac{\partial z^*}{\partial t} \times \frac{x_{Cr}^{\beta\gamma}\left(1 - x_C^{\gamma\beta}\right) - x_{Cr}^{\gamma\beta}\left(1 - x_C^{\beta\gamma}\right)}{V_m^\beta\left(1 - x_C^{\gamma\beta}\right)} \tag{2.13}$$

Rearranging Equations 2.9 and 2.13:

$$D_{Cr}^\gamma \frac{\bar{x}_{Cr}^\gamma - x_{Cr}^{\gamma\beta}}{V_m^\gamma \Delta z} = \frac{\partial z^*}{\partial t} \times \frac{x_{Cr}^{\beta\gamma}\left(1 - x_C^{\gamma\beta}\right) - x_{Cr}^{\gamma\beta}\left(1 - x_C^{\beta\gamma}\right)}{V_m^\beta\left(1 - x_C^{\gamma\beta}\right)} \tag{2.14}$$

By performing a thermodynamic calculation and solving Equation 2.14, the chromium concentration profile can be predicted. Stawström and Hillert's model takes into account the carbon activity in their thermodynamic calculation. However, the effect of multicomponent alloy in practice is not properly accounted in both thermodynamic and kinetic modelling. The interaction effect between nickel and chromium is neglected in the thermodynamic modelling and only diffusion fluxes of iron and chromium are considered in the kinetic modelling in this model.

2.5 Hall and Briant model

2.5.1 Thermodynamic Modelling

Hall and Briant (1984) [5] developed a simple thermodynamic model to determine the chromium concentration in matrix in equilibrium with carbide. An assumption is made in this model that the carbide is $Cr_{23}C_6$. The chromium concentration in matrix at the carbide–matrix interface is calculated based on the equilibrium reaction:

$$6\mathrm{C} + 23\mathrm{Cr} \rightleftarrows \mathrm{Cr}_{23}\mathrm{C}_6 \tag{2.15}$$

$$K_{eq} = \frac{1}{\left(\varphi_{Cr} c_{Cr}^{\gamma\beta}\right)^{23} a_C^6} \tag{2.16}$$

where K_{eq} is the equilibrium constant for carbide reaction, a_C is the activity of carbon in equilibrium with the carbide, $c_{Cr}^{\gamma\beta}$ is the chromium concentration in equilibrium with the carbide and φ_{Cr} is the activity coefficient of chromium.

In Hall and Briant's model, only the chromium and carbon activities are considered, therefore limiting again the model to Fe–Cr–C system.

2.5.2 Kinetic Modelling

The chromium concentration profiles are predicted based on bulk diffusion–controlled growth of a precipitate. Zener's theory is used in this model. The symmetric chromium–depletion profiles normal to the grain boundary can be well predicted by this model. However, the model does not account for any asymmetric profile as can be seen clearly in Figure 2.4. According to Hall and Briant, the asymmetric profiles were caused by grain boundary movement associated with the discontinuous precipitation of $\mathrm{Cr}_{23}\mathrm{C}_6$ carbides.

Hall and Briant managed to predict the chromium–depletion profile with this simple model. With the knowledge of this chromium concentration at the grain boundary region, the likelihood of sensitisation can be predicted. However, this model only managed to predict the symmetric chromium–depletion profiles but not the asymmetric profiles. Only chromium is considered in the thermodynamic calculation, the effect of multicomponent system in practice is neglected.

2.6 Was and Kruger model

2.6.1 Thermodynamic Modelling

Was and Kruger (1985) developed an integrated thermodynamic and kinetic model to describe the development of the chromium–depleted zone in Ni–Cr–Fe alloys. The model assumes that only $\mathrm{M}_7\mathrm{C}_3$ carbides are present along the grain boundary. As in Stawström and Hillert's model, the carbon activity is assumed to be spatially uniform at all times with local equilibrium at the carbide–matrix interface.

The free energy expression for the Ni–Cr–Fe–C system is according to Kohler [19] as:

$$G_\gamma = \sum_i x_i G_i^o + RT \sum_i x_i \ln x_i + \sum_{ij} \frac{x_i x_j}{x_i + x_j} \left(x_i h_{ij} + x_j l_{ji}\right) \tag{2.17}$$

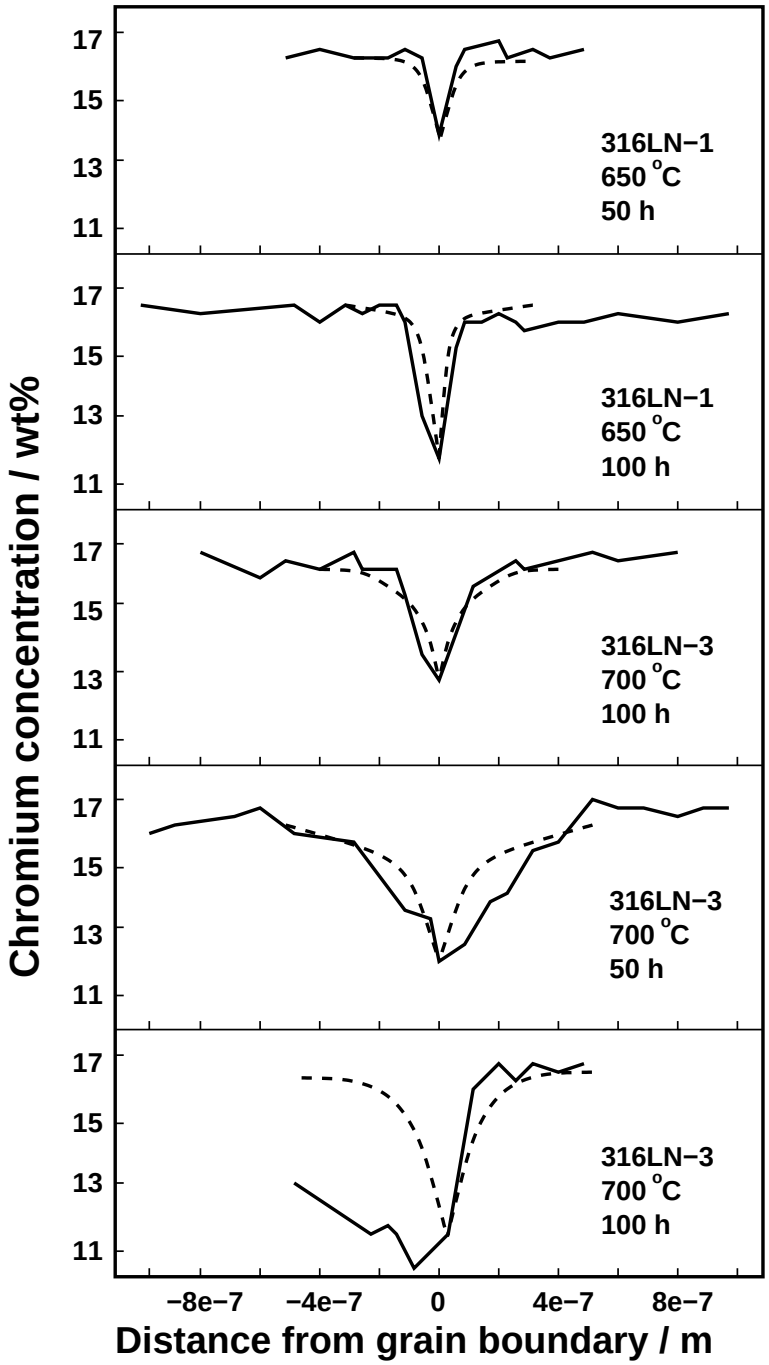

Figure 2.4: Comparison of measured and calculated (dashed line) chromium–depletion profile at the grain boundary region. After [5].

where x_i are mole fractions in the matrix phase, G_i^o the free energy of the pure element i in the austenite phase relative to its reference state, h_{ij} and l_{ji} are the binary interaction terms in which $i \neq j$.

The partial molar free energy of each element i is given by:

$$\begin{aligned}
\mu_i &= RT\ln x_i + G_i^o + \sum_{ij}\left(\frac{x_i x_j}{x_i + x_j}\right)\left[\left(\frac{x_i}{x_i + x_j}\right) + 1 - x_i\right] h_{ij} \\
&\quad + \sum_{ij} x_i \left[\left(\frac{x_j}{x_i + x_j}\right)^2 - \left(\frac{x_i x_j}{x_i + x_j}\right)\right] l_{ij} \\
&\quad - \sum_{jk}\left[h_{ik}\left(\frac{x_j^2 x_k}{x_j + x_k}\right) + h_{kj}\left(\frac{x_k^2 x_j}{x_j + x_k}\right)\right] \qquad (2.18) \\
\mu_i &= RT\ln a_i \qquad (2.19)
\end{aligned}$$

Rearranging Equations 2.18 and 2.19:

$$\begin{aligned}
RT\ln a_i &= RT\ln x_i + G_i^o \\
&\quad + \sum_{ij}\left(\frac{x_i x_j}{x_i + x_j}\right)\left[\left(\frac{x_i}{x_i + x_j}\right) + 1 - x_i\right] h_{ij} \\
&\quad + \sum_{ij} x_i \left[\left(\frac{x_j}{x_i + x_j}\right)^2 - \left(\frac{x_i x_j}{x_i + x_j}\right)\right] l_{ij} \\
&\quad - \sum_{jk}\left[h_{ik}\left(\frac{x_j^2 x_k}{x_j + x_k}\right) + h_{kj}\left(\frac{x_k^2 x_j}{x_j + x_k}\right)\right] \qquad (2.20)
\end{aligned}$$

where $i \neq j \neq k$, a_i is the activity of element i and G_i^o is the free energy of pure element i in the austenite phase relative to its reference state.

Was and Kruger realised that considering only binary interaction terms was not sufficient to accurately model the thermodynamics of carbide precipitation. A single ternary interaction parameter was introduced to model the quaternary Ni–Cr–Fe–C system. Due to the lack of experimental data, the quaternary system was approximated as a ternary system of Cr+(Ni+Fe)+C. The additional term for the free energy expression of the system was given by [10]:

$$G_{(additional)} = x_1 x_4 x' \Theta T \qquad (2.21)$$

where x_i are the mole fractions: x_1 = Cr, x_4 = C, x' = Ni + Fe and ΘT is the temperature dependent ternary interaction parameter in J mol^{-1}. Between 573 K to 1173 K, ΘT is given by [10]:

$$\Theta T = -118.86T + 202046.59 \text{ J mol}^{-1} \qquad (2.22)$$

The corresponding additional term to the partial molar free energies are [10]:

$$\begin{aligned}
\mu_{1(additional)} &= -x_1 x_4 x' \Theta T \qquad (2.23) \\
\mu_{4(additional)} &= x_1 x' (1 - x_4) \Theta T \qquad (2.24)
\end{aligned}$$

As in Hall and Briant's model, the equilibrium constant for carbide (Cr_7C_3) precipitation is given as:

$$K_{eq} = \frac{1}{(a_{Cr})^7 (a_C)^3} \tag{2.25}$$

where a_{Cr} and a_C are the chromium and carbon activities. The equilibrium constant K_{eq} can be obtained from:

$$\Delta G^o_{Cr_7C_3} = -RT \ln K_{eq} \tag{2.26}$$

where $\Delta G^o_{Cr_7C_3}$ is the Gibbs free energy of formation of Cr_7C_3. As the carbide in this model is taken to be composed solely by chromium and carbon, the mole fraction ratio of $\frac{Ni}{Fe}$ is a constant at any point. The total amount of mole fractions in the system is always equal to unity.

$$\frac{x_2}{x_3} = k \tag{2.27}$$

$$x_1 + x_2 + x_3 + x_4 = 1 \tag{2.28}$$

where k is a constant and x_i are the mole fractions: $x_1 = Cr$, $x_2 = Ni$, $x_3 = Fe$ and $x_4 = C$.

By solving Equations 2.20, 2.25, 2.27 and 2.28 simultaneously, the chromium concentration at the carbide–matrix interface can thus be determined. It is realised that the multicomponent effect is indeed important in modelling the thermodynamic of carbide precipitation. However, due to a lack of experimental data at that time, an approximation was made by introducing a single ternary term for a quaternary system.

2.6.2 Kinetic Modelling

Was and Kruger performed kinetic modelling to quantitatively describe the chromium–depleted zone adjacent to the grain boundary as a function of time at temperature, alloy composition and grain size. Fick's 2^{nd} law was discretized and solved numerically in this model.

Was and Kruger also discussed the effect of grain size on the chromium–depletion profile in their model. As the grain size is given as the sum of the diffusion spacing (Δm) of all nodes, therefore the chromium concentration which is numerically calculated is said to be grain size dependent:

$$g = \sum_{j=1}^{N} \Delta m(j) \tag{2.29}$$

The chromium concentration in the matrix at the carbide–matrix interface ($c_{Cr}^{\gamma\beta}$) rises with increasing time. As the precipitate grows, the carbon content in the matrix decreases, causing a decrease in its activity and thus increases the chromium activity in the matrix at the carbide–matrix interface. A smaller grain size gives a shorter diffusion path, thus approaching equilibrium more rapidly compared with a larger grain size. As shown in Figure 2.5, for the same length of time, a material with smaller grains gives a higher chromium concentration and achieves a flatter chromium profile earlier than larger grains.

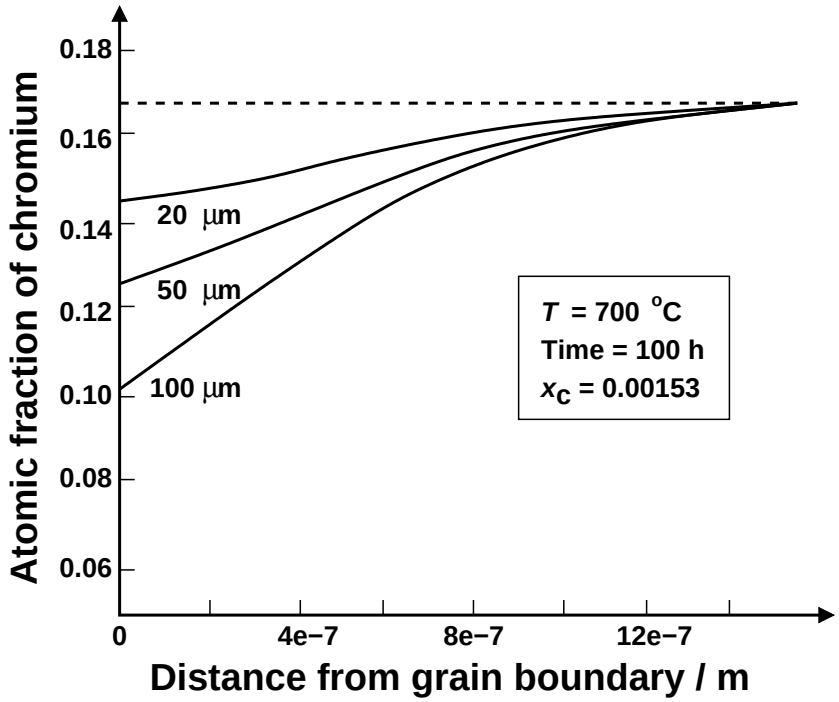

Figure 2.5: Effect of grain size on the chromium concentration profile after heat treating for 100 h at temperature 700 °C. x_C is the mole fraction of carbon. After [10].

Was and Kruger's model has a grain size effect. However, the development of chromium–depletion profile with time is modelled by considering only volume diffusion of chromium to the grain boundary but no other elements. In practice, multicomponent system is involved in precipitation reactions and the effect of multicomponent alloy may not be negligible.

2.7 Bruemmer model

2.7.1 Thermodynamic Modelling

Bruemmer (1990) [9] performed a thermodynamic calculation for carbide precipitation using the equilibrium Equation 2.15 as in Hall and Briant's model. Assuming

the precipitates are $Cr_{23}C_6$, the chromium concentration at the carbide–matrix interface is given as:

$$c_{Cr}^{\gamma\beta} = (K_{eq})^{-\frac{1}{23}}(\varphi_{Cr})^{-1}(\varphi_C c_C^{\gamma\beta})^{-\frac{6}{23}} \tag{2.30}$$

where φ_{Cr} and φ_C represent the activity coefficients of chromium and carbon, $c_C^{\gamma\beta}$ is the carbon concentration at the carbide–matrix interface. As carbon diffuses more rapidly than chromium, the carbon content is assumed to be equilibrated. The carbon content in the matrix at the carbide–matrix interface is assumed equal to the initial carbon content.

The above equation is justified for the 304 stainless steels, but not for the 316 stainless steels due to the presence of molybdenum. Molybdenum may incorporate into the $M_{23}C_6$ precipitates and become depleted during carbide growth. Therefore, the presence of molybdenum needed to be taken into account in thermodynamic calculation of carbide precipitation.

An effective chromium concentration that integrates molybdenum and chromium effects was developed by Fullman [20]:

$$\bar{c}_{Cr}^{*} = \bar{c}_{Cr}^{\gamma} + 0.35\bar{c}_{Mo}^{\gamma} \tag{2.31}$$

where $\bar{c}_{Cr}^{\gamma}$ and $\bar{c}_{Mo}^{\gamma}$ represent the initial chromium and molybdenum compositions of the steel. This effective chromium concentration term will directly influence the carbon and chromium activities at the interface. In order to calculate $c_{Cr}^{\gamma\beta}$, all the parameters in Equation 2.30 has to be determined. The carbon activity coefficient (φ_C) is given by [9]:

$$\begin{aligned} \ln\varphi_C &= -1.845 + \frac{5100}{T} + \left[\bar{c}_C^{\gamma}\left(\frac{11}{92} - \frac{6330}{T}\right)\right] - \left[\bar{c}_{Ni}^{\gamma}\left(2.2 - \frac{7600}{T}\right)\right] \\ &\quad + \left[\bar{c}_{Cr}^{*}\left(24.4 - \frac{38400}{T}\right)\right] - \left[(\bar{c}_{Cr}^{*})^2 - \left(96.8 - \frac{84800}{T}\right)\right] \end{aligned} \tag{2.32}$$

where T is temperature in K, $\bar{c}_C^{\gamma}$ and $\bar{c}_{Ni}^{\gamma}$ are the initial compositions of carbon and nickel in wt%. The equilibrium constant can be calculated with:

$$\Delta G^{o}_{M_{23}C_6} = -RT\ln K_{eq} \tag{2.33}$$

where $\Delta G^{o}_{M_{23}C_6}$ is the Gibbs free energy of carbide formation given as [9]:

$$\Delta G^{o}_{M_{23}C_6} = -98280 - 9.2T \quad \text{J mol}^{-1} \tag{2.34}$$

An empirical relation was developed [9] for the activity coefficient of chromium. This relation was defined by direct measurements of the chromium–depletion region:

$$\varphi_{Cr} = 10.55 - 94.84T_n + 282.9T_n^2 - 242.8T_n^3 \tag{2.35}$$

where $T_n = \frac{T}{2000}$ for 304 stainless steels, $T_n = \frac{(T-30)}{2000}$ for 316 stainless steels and T is temperature given in K.

The chromium concentration at the carbide–matrix interface is thus calculated. A comparison is made between the predictions of minimum chromium concentration at the carbide–matrix interface by Stawström and Hillert [8], Fullman [20] and Bruemmer's model [9] as shown in Figure 2.6. By using the empirical relation defined by direct measurements at the chromium–depletion region, Bruemmer's prediction of minimum chromium concentration at the carbide–matrix interface is not surprisingly the best among all as can be seen in Figure 2.6. Although the effect of molybdenum is considered in this model by introducing an effective chromium concentration term, but the effects of other elements such as nickel and manganese are still not taken into account.

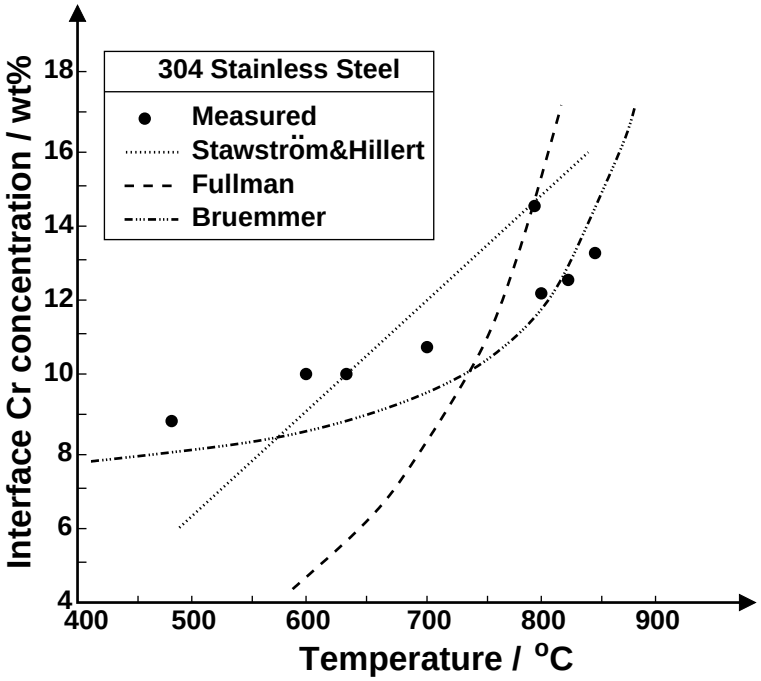

Figure 2.6: Comparison of measured and predicted minimum chromium concentration in the matrix at the carbide–matrix interface ($c_{Cr}^{\gamma\beta}$) as a function of the heat–treatment temperature. After [9].

2.7.2 Kinetic Modelling

Bruemmer developed a theoretically based, empirically modified kinetic model to predict chromium–depletion characteristics and degree of sensitisation. The methodology used in this model is shown in Figure 2.7.

Carbide precipitation is assumed to occur as a continuous film along grain boundaries in this model. The chromium concentration at the carbide–matrix interface is determined based on the thermodynamics of carbide formation with some empirical modifications as discussed earlier.

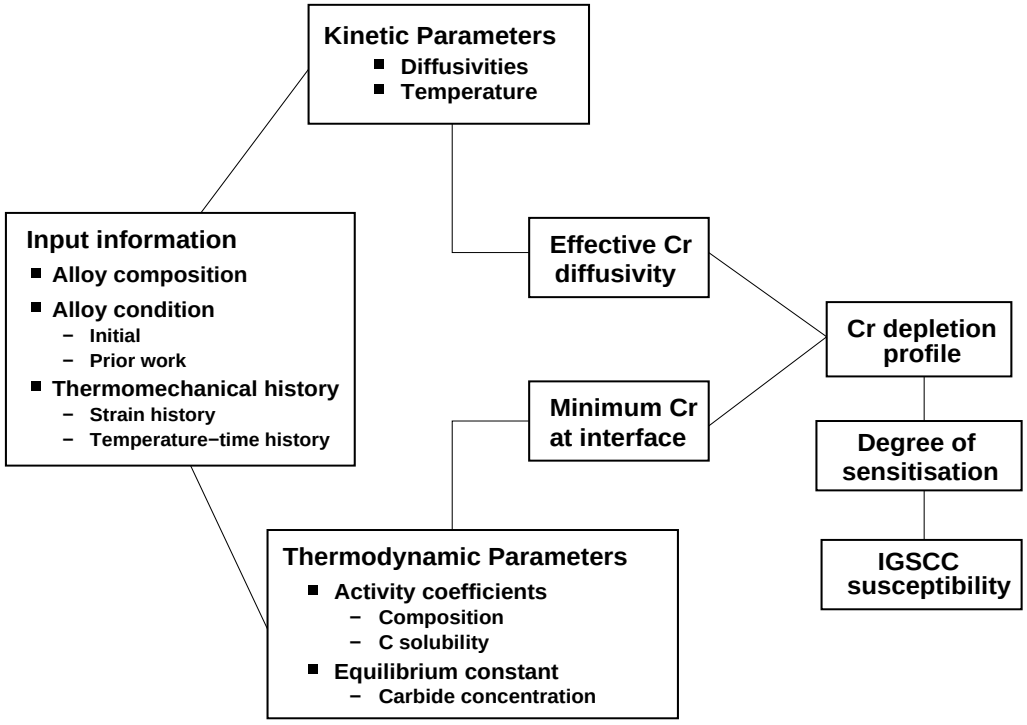

Figure 2.7: Flow diagram showing basic methodology of Bruemmer model. IGSCC is intergranular stress corrosion cracking. After [9].

The chromium–depletion kinetics at the grain boundary are modelled as in the Strawström and Hillert [8] theory. The critical chromium–depletion width can be determined if the critical chromium concentration at the carbide–matrix interface, $c^{\gamma\beta}_{Cr(critical)}$, is known.

$$W_{(critical)} = 2\sqrt{D^{\gamma}_{Cr}t}\frac{c^{\gamma\beta}_{Cr(critical)} - c^{\gamma\beta}_{Cr}}{\bar{c}^{\gamma}_{Cr} - c^{\gamma\beta}_{Cr}} \tag{2.36}$$

where $\bar{c}^{\gamma}_{Cr}$ is the bulk chromium concentration, $c^{\gamma\beta}_{Cr}$ is the chromium concentration in the matrix in equilibrium with the carbide, D^{γ}_{Cr} the chromium diffusivity and t is time.

Bruemmer's theoretically based and empirically modified model is able to quantitatively predict degree of sensitisation. Although Bruemmer has considered the effect of molybdenum in the thermodynamic calculation, the effect of other elements such as nickel is not accounted for. As in the previous models, no proper multicomponent effects are considered in modelling the kinetics of precipitation.

2.8 Mayo model

A semi–empirical model was established by Mayo (1997) [11] to model the chromium–depletion at the grain boundary over a wide range of temperatures and thermal treatment time for Ni–Cr–Fe alloys. Mayo argued that by assuming the chromium concentration in matrix at the carbide–matrix interface, $c_{Cr}^{\gamma\beta}$, instantaneously reaches a minimum, as in the previous work [5, 10], is incorrect. A finite time is required for carbide nucleation kinetics and the establishment of the depletion zone. Thus, t_c is defined as the holding time to reach the minimum chromium concentration in the matrix at the carbide–matrix interface, $c_{Cr(min)}^{\gamma\beta}$.

The kinetics of precipitation are modelled based on conventional diffusion equations solved by a numerical method. An isoconcentration contour plot as a function of annealing time and temperature was generated based on these calculations to identify regions likely to sensitise. The chromium concentration profile as a function of the diffusion time is expressed by an error function [11]:

$$c(z,t) = c_{Cr}^{\gamma\beta} + \left(\bar{c}_{Cr}^{\gamma} - c_{Cr}^{\gamma\beta}\right) \operatorname{erf}\left(\frac{z}{2\sqrt{D^{\gamma}t}}\right) \tag{2.37}$$

where $\bar{c}_{Cr}^{\gamma}$ is the initial chromium concentration, $c_{Cr}^{\gamma\beta}$ is the chromium concentration in the matrix at the carbide–matrix interface at time t and D^{γ} is the bulk diffusivity.

Based on Zener's formula, the isothermal carbide growth radius is approximated as:

$$r = \Gamma\sqrt{D^{\gamma}t} \tag{2.38}$$

where Γ is a constant.

In carbide growth theory, the chromium that enters the carbide must equal that which has been depleted in the matrix. By assuming the weight fraction of Cr in Cr_7C_3 carbides as 0.91, the chromium concentration in the matrix can be calculated:

$$0.91\Gamma\sqrt{D^{\gamma}t} = \left(\bar{c}_{Cr}^{\gamma} - c_{Cr}^{\gamma\beta}\right) \int_0^z \left[1 - \operatorname{erf}\left(\frac{z}{2\sqrt{D^{\gamma}t}}\right)\right] dz \tag{2.39}$$

By using existing data from the literature [21, 22, 23, 24] for Alloy 600 with nominal composition of 16 wt% Cr and 0.03 wt% C, the chromium concentration in the matrix in equilibrium with the precipitate phase can be calculated with this empirical equation [11]:

$$c_{Cr}^{\gamma\beta} = c_{Cr(min)}^{\gamma\beta} + \left(4.72 \times 10^{-4}t - 0.356\right) \exp\left[\frac{325.7t - 3.5027 \times 10^{-5}}{t - t_c}\right] \text{ wt\%} \tag{2.40}$$

$$c^{\gamma\beta}_{Cr(min)} = \bar{c}^{\gamma}_{Cr} - \left\{ \frac{\bar{c}^{\gamma}_{C}}{\bar{c}^{\gamma}_{Cr}} \left(0.0823t - 68.01\right) \times \frac{T\log\left(-720t + 7.36560 \times 10^{5}\right)}{10^{3}} \right\} \text{ wt\%} \tag{2.41}$$

where $c^{\gamma\beta}_{Cr(min)}$ is the minimum chromium concentration in the matrix in equilibrium with the precipitate phase at temperature T in K, $\bar{c}^{\gamma}_{C}$ is the initial carbon content in matrix and t_c is the holding time to reach $c^{\gamma\beta}_{Cr(min)}$, given as:

$$t_c = \exp\left[\frac{2.303\bar{c}^{\gamma}_{Cr}\left(\bar{c}^{\gamma}_{Cr} - c^{\gamma\beta}_{Cr(min)}\right)}{\bar{c}^{\gamma}_{Cr}\left(0.0823T - 68.01\right)T} \right] \text{ h} \tag{2.42}$$

where $\bar{c}^{\gamma}_{Cr}$ is the initial carbon concentration. The constants in these equations were obtained from literature.

A computer simulation is used to compute $c^{\gamma\beta}_{Cr(min)}$ and also $c^{\gamma\beta}_{Cr}$ for various time and temperature. With the $c^{\gamma\beta}_{Cr}$ value, the chromium concentration profile can then be calculated using Equation 2.37. The process of the simulation is as described in the flow chart (Figure 2.8).

The results obtained with Mayo's model can be said in good agreement with experimental data. Figure 2.9 shows a comparison of the experimental data and the prediction results of Mayo's model. The results obtained by Was and Kruger [10] using integrated thermodynamic and kinetic model are used for comparison, Figure 2.10.

Figure 2.11 is the time–temperature–concentration (TTC) contour plot based on the predicted $c^{\gamma\beta}_{Cr(min)}$ values using Mayo's model. Although this model manages to predict a better result compared with Was and Kruger, yet still no effect of multicomponent system is taken into account in this model.

2.9 Sahlaoui *et al.* model

Sahlaoui *et al.* (2002) [12] argued that the assumptions of instantaneous cabide nucleation and that the chromium content in the matrix at the carbide–matrix interface instantaneously reaches its thermodynamic equilibrium value made in previous models [8, 10, 25] are the main cause of their result discrepancies. Thus, they developed a two–stage diffusional model for Ni–Cr–Fe alloys which takes into account dechromization and rechromization.

According to Sahlaoui *et al.*, the dechromization stage begins when the nucleation and growth of chromium carbides start at time τ as shown in Figure 2.12. When the chromium concentration in the matrix at the carbide–matrix interface reaches a critical value $c^{\gamma\beta}_{Cr(critical)}$ after annealing duration t_s at temperature T, sensitisation

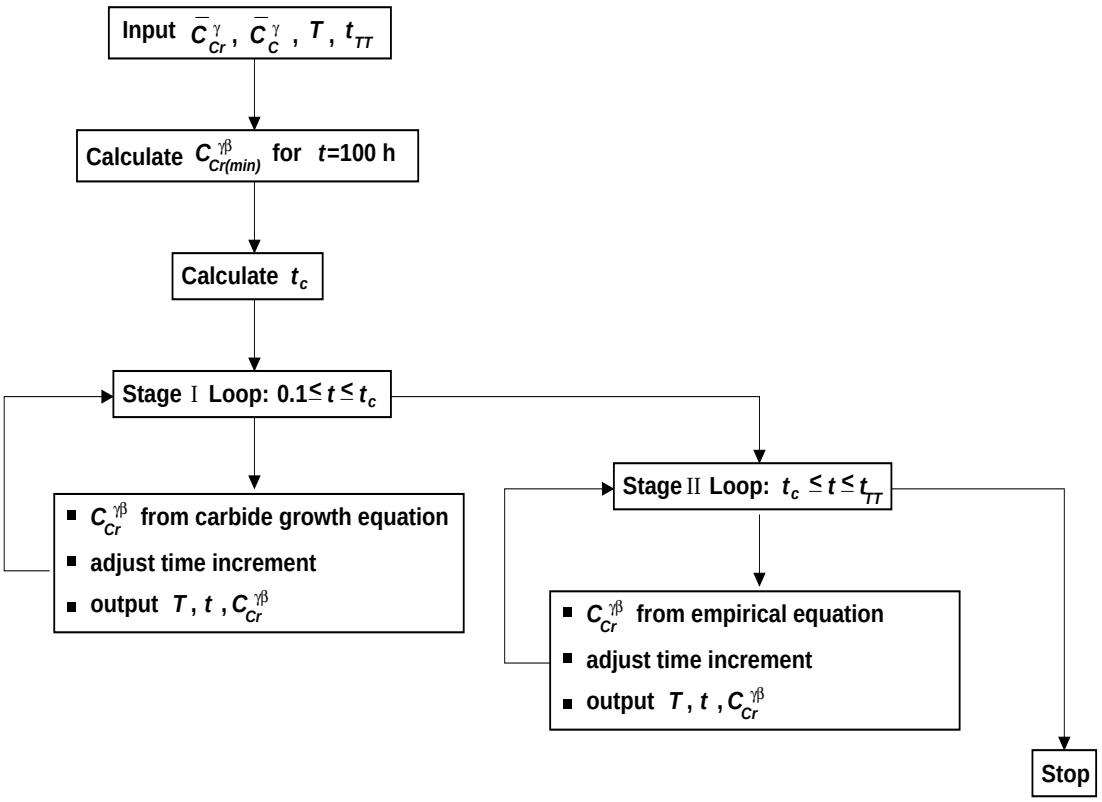

Figure 2.8: Flow chart illustrated the process to calculate the $c_{Cr}^{\gamma\beta}$ as a function of time in Mayo's model. t_{TT} is thermal treatment time. After [11].

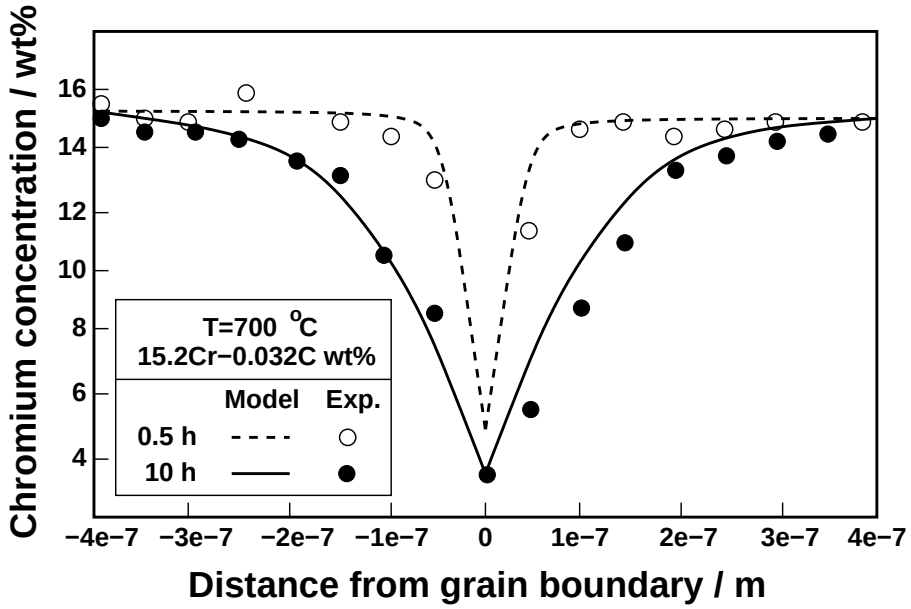

Figure 2.9: Comparison of experimental and predicted results of Mayo's model for chromium–depletion. After [11].

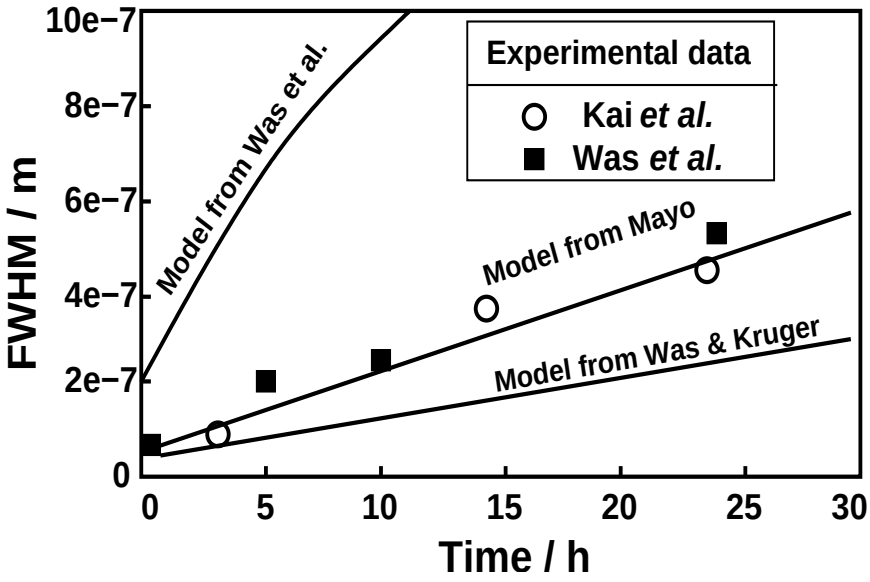

Figure 2.10: Comparison of predicted results of chromium–depletion zone halfwidth (FWHM) between Was and Kruger model and Mayo model. After [11].

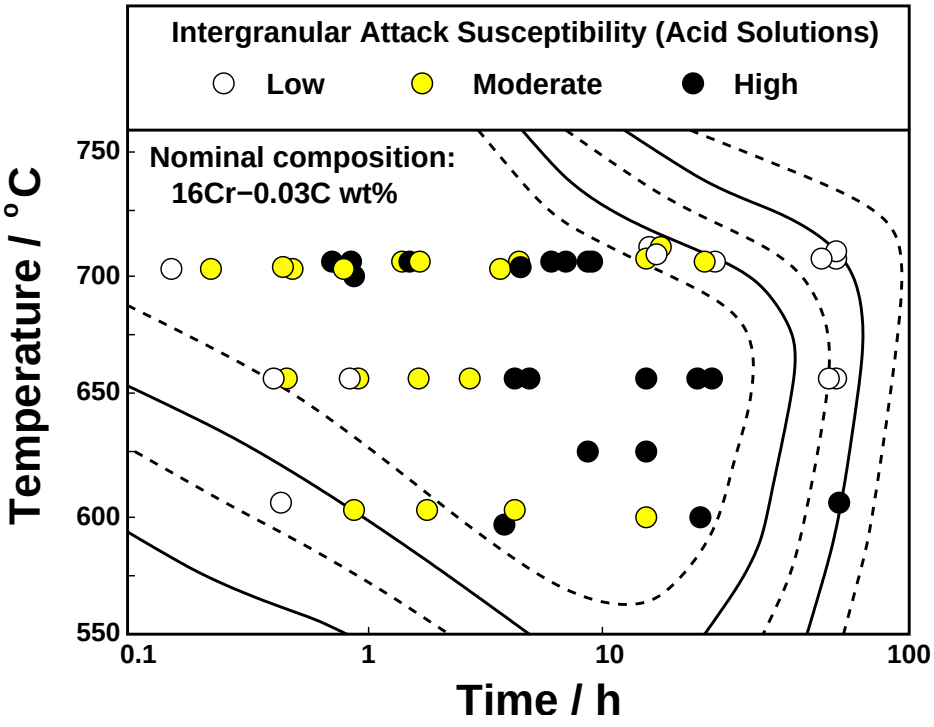

Figure 2.11: Time–temperature–concentration (TTC) contour plot based on the calculated $c^{\gamma\beta}_{Cr(min)}$ values to predict regions susceptible to sensitisation. After [11].

begins. The chromium concentration in the matrix continues to decrease until a minimal value $c^{\gamma\beta}_{Cr(min)}$ which corresponds to a partial thermodynamic equilibrium between carbides and matrix.

Carbon atoms diffuse very fast compared with chromium leading to a uniform de-

crease of carbon concentration with depth, leading to an increase in local chromium activity, causing rechromization. Desensitisation is obtained when the chromium level in the matrix at the interface reaches the critical value after time t_d.

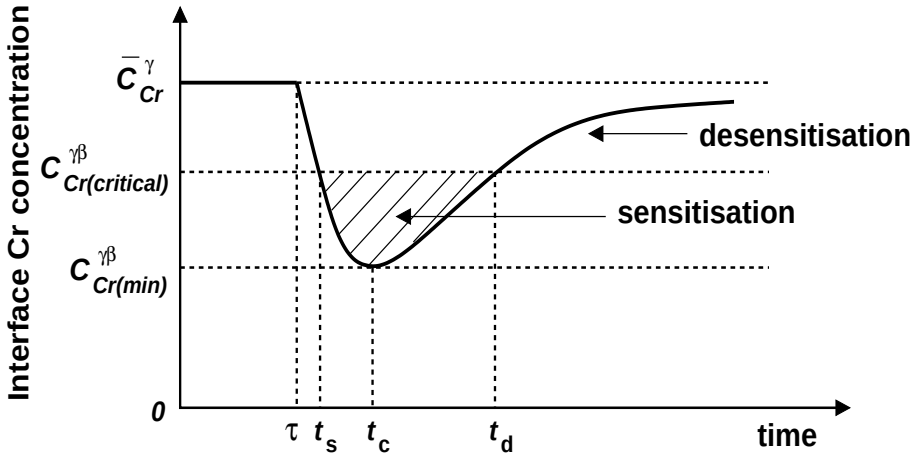

Figure 2.12: Influence of chromium concentration in the matrix at the carbide–matrix interface on the process of sensitisation–desensitisation during aging. After [12].

2.9.1 Dechromization stage

In this model, the chromium concentration in the matrix at the carbide–matrix interface, $c^{\gamma\beta}_{Cr}$, during dechromization stage as shown in Figure 2.13 is given by [12]:

$$c^{\gamma\beta}_{Cr} = \bar{c}^{\gamma}_{Cr} \exp\left(-k_1 \frac{t}{t_c}\right) \tag{2.43}$$

where $\bar{c}^{\gamma}_{Cr}$ is the initial chromium content, t_c is the duration to reach $c^{\gamma\beta}_{Cr}$ and k_1 is a constant.

With the $c^{\gamma\beta}_{Cr}$ value, the chromium concentration profile in the depleted zone can be calculated using Fick's 2^{nd} law as in Mayo's model.

$$c(z,t) = c^{\gamma\beta}_{Cr} + \left(\bar{c}^{\gamma}_{Cr} - c^{\gamma\beta}_{Cr}\right) \text{erf}\left(\frac{z}{2\sqrt{D^{\gamma}t}}\right) \tag{2.44}$$

where z is the distance from the carbide–matrix interface into the matrix, t is time, D^{γ} is the diffusion coefficient and $\bar{c}^{\gamma}_{Cr}$ is the initial chromium concentration.

2.9.2 Rechromization stage

At the rechromization stage (stage d) as shown in Figure 2.13, $c^{\gamma\beta}_{Cr}$ is analytically calculated based on the conservation of matter flows through the carbide–matrix interface leads to the equality of the two areas S_1 and S_2. Sahlaoui *et al.* assumed

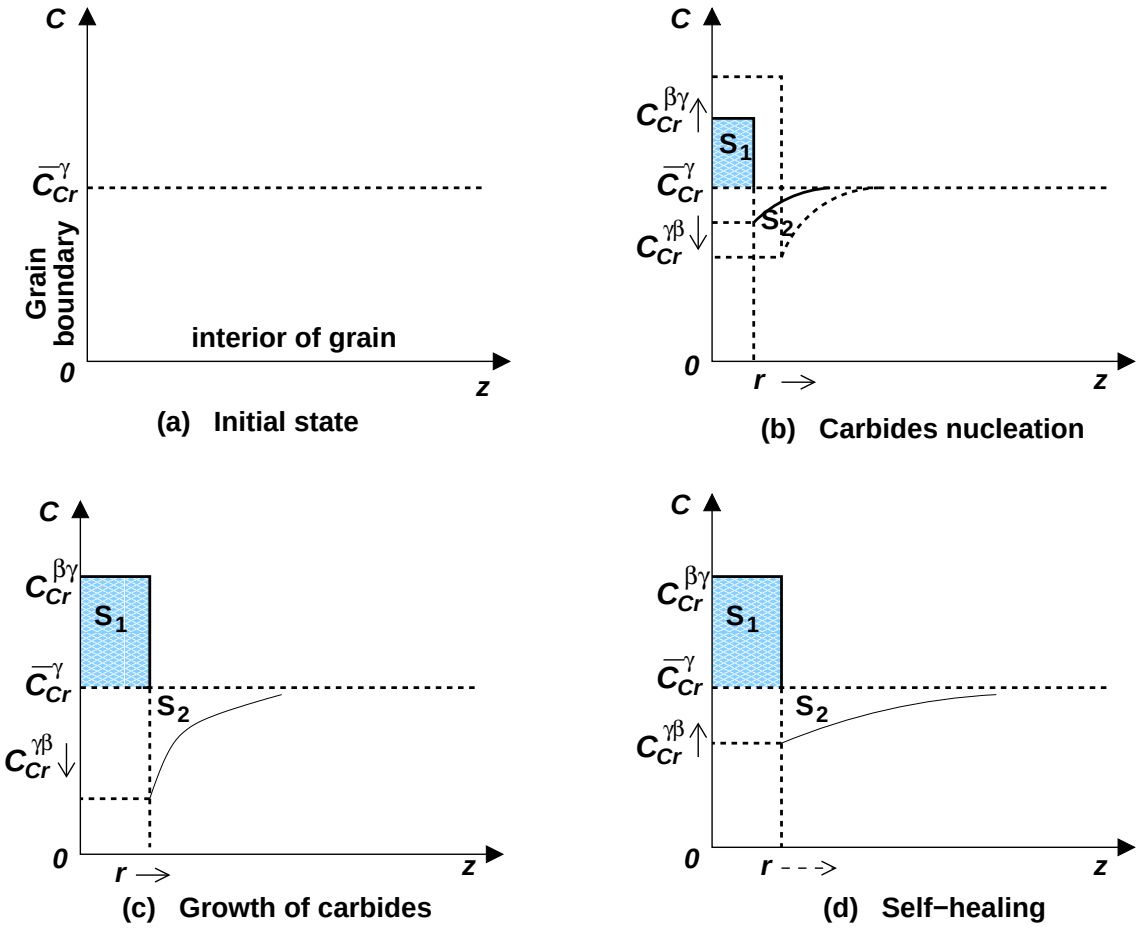

Figure 2.13: Chromium concentration profile during aging. After [12].

the growth of carbides is sufficiently slowed down to be neglected at time t_c and the size of carbide can be considered as constant. Thus the area S_1 is given by:

$$S_1 = c_{Cr}^{\beta\gamma} \Gamma \sqrt{D^{\gamma} t_c} \tag{2.45}$$

where Γ is a constant and D^{γ}_{Cr} is the chromium diffusion coefficient which depends on temperature. The area S_2 is approximated with the assumption of linear chromium concentration gradient near the grain boundaries.

$$S_2 = \frac{\left(\bar{c}^{\gamma}_{Cr} - c^{\gamma\beta}_{Cr}\right) W}{2} \tag{2.46}$$

where W is the width of the depleted zone. Based on the random–walk theory by Stawström and Hillert [8], the width can be approximated as:

$$W \approx 2\sqrt{D^{\gamma} t} \tag{2.47}$$

The substitution of W gives:

$$c_{Cr}^{\gamma\beta} = \bar{c}_{Cr}^{\gamma} - c_{Cr}^{\beta\gamma}\Gamma\sqrt{\frac{t_c}{t}} \tag{2.48}$$

As the growth of carbides is assumed to be sufficiently slow to be neglected at this stage, Sahlaoui *et al.* calculated the chromium concentration profile based on interdiffusion mechanism through Matano plane, a plane that divides the depleted zone into two equal areas in which the transport of the chromium atoms across the two areas takes place without accumulation, given as:

$$c(z,t) = \frac{1}{2}\left(c_{Cr}^{\gamma\beta} - \bar{c}_{Cr}^{\gamma}\right)\operatorname{erfc}\left(\frac{z}{2\sqrt{D^{\gamma}t}}\right) + \bar{c}_{Cr}^{\gamma} \tag{2.49}$$

Sahlaoui *et al.* assumed that the precipitation has already finished when self–healing process begins. No thermodynamic calculations are discussed in the model and the obtaining of $c_{Cr}^{\beta\gamma}$ value is not indicated. The neglection of carbide growth during the self–healing stage may cause thermodynamic instability at the carbide–matrix interface, leading to inaccuracy in the predictions of the chromium concentration profile in the matrix.

2.10 Summary

Previous attempts on modelling grain boundary precipitation and prediction of sensitisation have been reviewed. The importance of local equilibrium at the carbide–matrix interface during precipitation has been indicated by some authors in the thermodynamic modelling. Assumptions are made to reduce a multicomponent problem into a pseudo–binary system in some models. Although Was and Kruger realised the importance of multicomponent effects in modelling precipitation, due to lack of experimental data, an approximation was made in their calculations. Mayo and Sahlaoui *et al.* assumed that the chromium concentration in the matrix at the carbide–matrix interface do not achieve a minimum instantaneously during precipitation and also the growth of carbides is sufficiently slowed to be neglected during self–healing process. These assumptions may cause thermodynamic instability and further lead to inaccuracy in the predictions of the chromium concentration profiles. Thus, it would be useful to develop a new model, avoiding unnecessary approximations and properly taking into account the effects of multicomponent systems.

Chapter 3

Modelling of Sensitisation

Considerable research has been conducted in the past to model grain boundary precipitation, as discussed in the previous chapter. However, these models are not suitable for practical purposes as some of them do not account for multicomponent reactions. Furthermore, some of the models contain parameters which are difficult to obtain, such as quaternary interaction terms and thus approximations have to be made in the calculations. In this work, an attempt is made to create a general physical model with minimum approximations to predict sensitisation in austenitic stainless steels.

3.1 MTDATA

An accurate thermodynamic calculation is needed to model the kinetics of grain boundary precipitation. Hence, a software known as MTDATA (Metallurgical and Thermochemical DATAbank) is used in this work to perform thermodynamic calculations. MTDATA is a Gibbs free energy minimisation algorithm which uses the SGTE (Scientific Group Thermodata Europe) or other appropriate thermodynamic databases. This software or data package is useful in predicting the complex equilibria in multicomponent multiphase systems [26].

Most of the previous work on sensitisation used phase *diagrams* in their calculations. However, phase diagrams are generally suitable for picturing binary or ternary systems. In practice, grain boundary precipitation in austenitic stainless steels involves multicomponent systems. The CALPHAD (CALculation of PHAse Diagram) method [27] can readily deal with the behaviour of complex multicomponent systems. For any given system for which appropriate thermodynamic data exist, MTDATA can calculate the equilibrium composition and weight fraction of the phases present by the minimisation of Gibbs energy.

Although MTDATA is able to predict thermodynamic properties, time–dependent parameters require kinetic theory. Hence, it would be useful to develop a physical model which interfaces with MTDATA to generate useful thermodynamic information such as the interface compositions or the chemical potential of each element to

be implemented in the kinetics of sensitisation.

3.2 Atomic Mobilities

The thermodynamic information evaluated from MTDATA is used as an input in the modelling of multicomponent diffusion. The diffusion flux of an element i is given by [28]:

$$J_i^L = -c_i M_i \nabla \mu_i \tag{3.1}$$

where J_i^L is the diffusional flux of element i relative to the lattice–fixed frame of reference (f.o.r.), c_i is the concentration of element i, M_i the mobility of element i and $\nabla \mu_i$ is the gradient in chemical potential of element i.

Andersson and Ågren [29] expressed the atomic mobility in a multicomponent system as a function of the temperature and composition. For an element i in a given phase, the mobility M_i is given by:

$$M_i = M_i^o \frac{1}{RT} \exp \frac{-Q_i}{RT} \tag{3.2}$$

where M_i^o is a frequency factor, R is the gas constant, T is the temperature and Q_i is an activation energy. In this work, the mobility data for the diffusion of iron in the face–centered–cubic (fcc) phase in the Fe–Cr–Ni systems were obtained from the published literature [30, 31] as:

$$\begin{aligned} M_{\mathrm{Fe}} &= \frac{1}{RT}\{3.202 \times 10^{-4} x_{\mathrm{Fe}} + 3.164 \times 10^{-4} x_{\mathrm{Ni}} + 2.364 \times 10^{-4} x_{\mathrm{Cr}}\} \times \\ &\quad \exp\left[\frac{-(35880 x_{\mathrm{Fe}} + 34410 x_{\mathrm{Ni}} + 36130 x_{\mathrm{Cr}})}{T}\right] \mathrm{m^2 J^{-1} s^{-1} mol^{-1}} \end{aligned} \tag{3.3}$$

$$\begin{aligned} M_{\mathrm{Ni}} &= \frac{1}{RT}\{1.111 \times 10^{-4} x_{\mathrm{Fe}} + 3.808 \times 10^{-4} x_{\mathrm{Ni}} + 1.542 \times 10^{-4} x_{\mathrm{Cr}}\} \times \\ &\quad \exp\left[\frac{-(35650 x_{\mathrm{Fe}} + 34600 x_{\mathrm{Ni}} + 38010 x_{\mathrm{Cr}})}{T}\right] \mathrm{m^2 J^{-1} s^{-1} mol^{-1}} \end{aligned} \tag{3.4}$$

$$\begin{aligned} M_{\mathrm{Cr}} &= \frac{1}{RT}\{2.747 \times 10^{-4} x_{\mathrm{Fe}} + 1.117 \times 10^{-4} x_{\mathrm{Ni}} + 1.444 \times 10^{-4} x_{\mathrm{Cr}}\} \times \\ &\quad \exp\left[\frac{-(36100 x_{\mathrm{Fe}} + 32080 x_{\mathrm{Ni}} + 34620 x_{\mathrm{Cr}})}{T}\right] \mathrm{m^2 J^{-1} s^{-1} mol^{-1}} \end{aligned} \tag{3.5}$$

where x_{Fe}, x_{Ni} and x_{Cr} are the mole fractions of iron, nickel and chromium.

Jönsson [32] presented an expression for mobility of carbon in fcc C–Cr–Fe–Ni alloys as:

$$M_{\mathrm{C}} = M^o \frac{1}{RT} \exp\left(\frac{-Q_{\mathrm{C}}}{RT}\right) = \frac{1}{RT} \exp\left(\frac{\Delta G_{\mathrm{C}}^*}{RT}\right) \tag{3.6}$$

where M^o is a frequency factor, $Q_{\rm C}$ is an activation energy, $M^o = \exp(\Phi_{\rm C})$ and $\Delta G^*_{\rm C} = RT\Phi_{\rm C} - Q_{\rm C}$ where $\Phi_{\rm C}$ is a composition dependency parameter. The CALPHAD method is used to model the composition dependent mobility by fitting the quantity $\Delta G^*_{\rm C}$ with a sublattice model. In practice, different components mix on different sublattices. For example, in austenite, carbon, nitrogen and boron mix on the interstitial sublattice while iron, chromium, nickel and other substitutional elements mix on the substitutional sublattice. Therefore a sublattice model is introduced to allow the use of many sublattices and concentration dependent terms [27].

$$\begin{aligned}\Delta G^*_{\rm C} &= \sum_i \sum_j y_i y_j \Delta G^{*\ i:j}_{\rm C} \\ &+ \sum_i \sum_{j>i} \sum_l y_i y_j y_l \left(\sum_r {}^r\Delta G^{*\ i,j:l}_{\rm C} (y_i - y_j)^r \right) \\ &+ \sum_i \sum_l \sum_{m>l} y_i y_l y_m \left(\sum_r {}^r\Delta G^{*\ i:l,m}_{\rm C} (y_l - y_m)^r \right) \end{aligned} \tag{3.7}$$

where the indices separated by a colon indicate which element occupies different sublattices. For example, $\Delta G^{*\ \rm Fe:Va}$ shows Fe is on the first sublattice with a vacancy on the second sublattice. $\Delta G^{*\ \rm Cr,Ni:Va}$ indicates an interaction parameter for Cr and Ni on the first sublattice with a vacancy on the second one. y_i is the fraction of the sites occupied by element i on its sublattice. The individual parameters $\Delta G^{*\ i:j}_{\rm C}$ are expressed as a function of temperature. All the parameters needed for the calculation of the carbon mobility including the influence of other substitutional elements on carbon mobility in austenite for Fe–Cr–Ni–C alloys can be obtained from the published literature by Jönsson [32].

A FORTRAN (formula translation) program is written in this work to calculate the mobilities for all substitutional and interstitial elements involved in grain boundary precipitation in austenitic stainless steels.

3.3 Identification of the Flux–balance Tie–line

Most of the previous attempts [5, 8, 10, 11, 12] in modelling carbide precipitation in austenitic stainless steels used the binary theory of diffusion–controlled precipitate growth. This theory, however, is only suitable for binary alloys and does not account for different effects in multicomponent systems. The concentration profile in this theory is often determined by the mass–balance tie–line of the equilibrium phase diagram. However, different elements involved in the precipitation process can have vastly different diffusivities. For example, the diffusivity of carbon is several orders of magnitude larger than that of chromium in austenite. Hence, the mass–balance tie–line method, which gives different values of the interface velocity for different elements, is no longer applicable.

3.3.1 Flux–balance Theory

Previous studies by Coates [33, 34] have suggested a flux–balance method to solve the diffusion equations for multicomponent systems whilst maintaining local equilibrium at the interface. In this discussion, a ternary system is considered as an example, but the method can be applied to multicomponent systems. For a ternary system in which the precipitate β is in equilibrium with the matrix γ, the following set of flux equations has to be satisfied to obtain a unique interface velocity v:

$$J_1 = v\left(c_1^{\beta\gamma} - c_1^{\gamma\beta}\right) \tag{3.8}$$

$$J_2 = v\left(c_2^{\beta\gamma} - c_2^{\gamma\beta}\right) \tag{3.9}$$

where J is the flux and the subscripts refer to the elements. As mentioned before, the mass–balance tie–line method is no longer applicable as it gives different values of velocity for different elements. A tie–line fixed based on Equations 3.8 and 3.9 is known as flux–balance tie–line method and is used in this model.

As the diffusivity of interstitial element is several orders of magnitude higher than that of the substitutional solute, it is generally incorrect to select a tie–line that passes through E, which is the bulk composition, to determine the interface compositions in a multicomponent system [35]. Thus an alternative tie–line is chosen to maintain local equilibrium at the interface by either minimising the concentration gradient of interstitial element such as carbon or maximising the gradient of substitutional element to compensate for its small diffusivity. Figure 3.1 shows the difference between the flux–balance fixed tie–line and the mass–balance fixed tie–line. It is clear that the mass–balance tie–line that goes through E is in general different compared with the flux–balance tie–line that passes through F.

3.3.2 Flux–balance Tie–line

The conventional flux of element i in a multicomponent system is given as:

$$J_i = -D_i \nabla c_i - \sum_{j \neq i} D_{ij} \nabla c_j \tag{3.10}$$

where $D_{ij}\nabla c_j$ is the cross–diffusion term which arises because of the chemical potential change of element i due to the gradient of the other components. Previous attempts have made assumptions that the cross–diffusion term is negligible. At the point where there is almost no carbon concentration gradient, there is still a steep gradient of chromium concentration. Even if $D_{CCr} \ll D_C$, it is not necessarily that $D_{CCr}\nabla c_{Cr} \ll D_C \nabla c_C$ because $\nabla c_{Cr} \gg \nabla c_C$, which means the flux of carbon may not be absent.

In order to exploit the chemical potential of each element, it is more convenient to express the flux as:

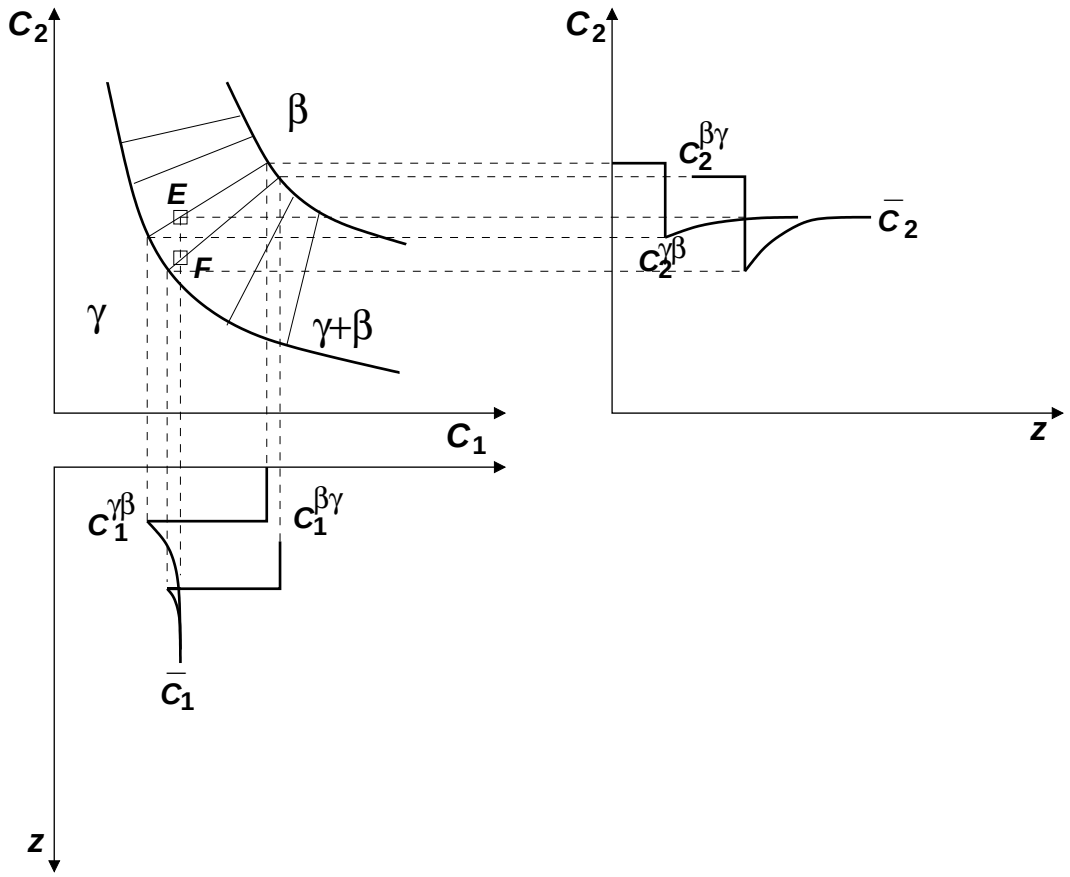

Figure 3.1: Diagram showing the flux–balance tie–line (passes through F) and the mass–balance tie–line (passes through E). The subscripts refer to the elements [36].

$$J_i = -c_i M_i \nabla \mu_i \tag{3.11}$$

where c_i is the concentration of element i and M_i is its mobility. By dealing directly with the chemical potential of each element, the cross–diffusion effects are naturally taken into account. MTDATA is thus used to perform thermodynamic calculations in this model.

A FORTRAN program has been written to interface with MTDATA to determine the flux–balance tie–line. The algorithm for finding the flux–balance tie–line is described in Figure 3.2. It is assumed that the carbon activity is uniform in the matrix as the mobility of carbon is very large relative to other substitutional elements. Therefore, a tie–line in which the activity of carbon at the interface is almost equal to the far–field carbon activity is first determined. When this tie–line is found, the velocity of the interface is calculated from the profile of each substitutional element. The aim here is to find the flux–balance tie–line with a unique interface velocity for all substitutional elements in the system.

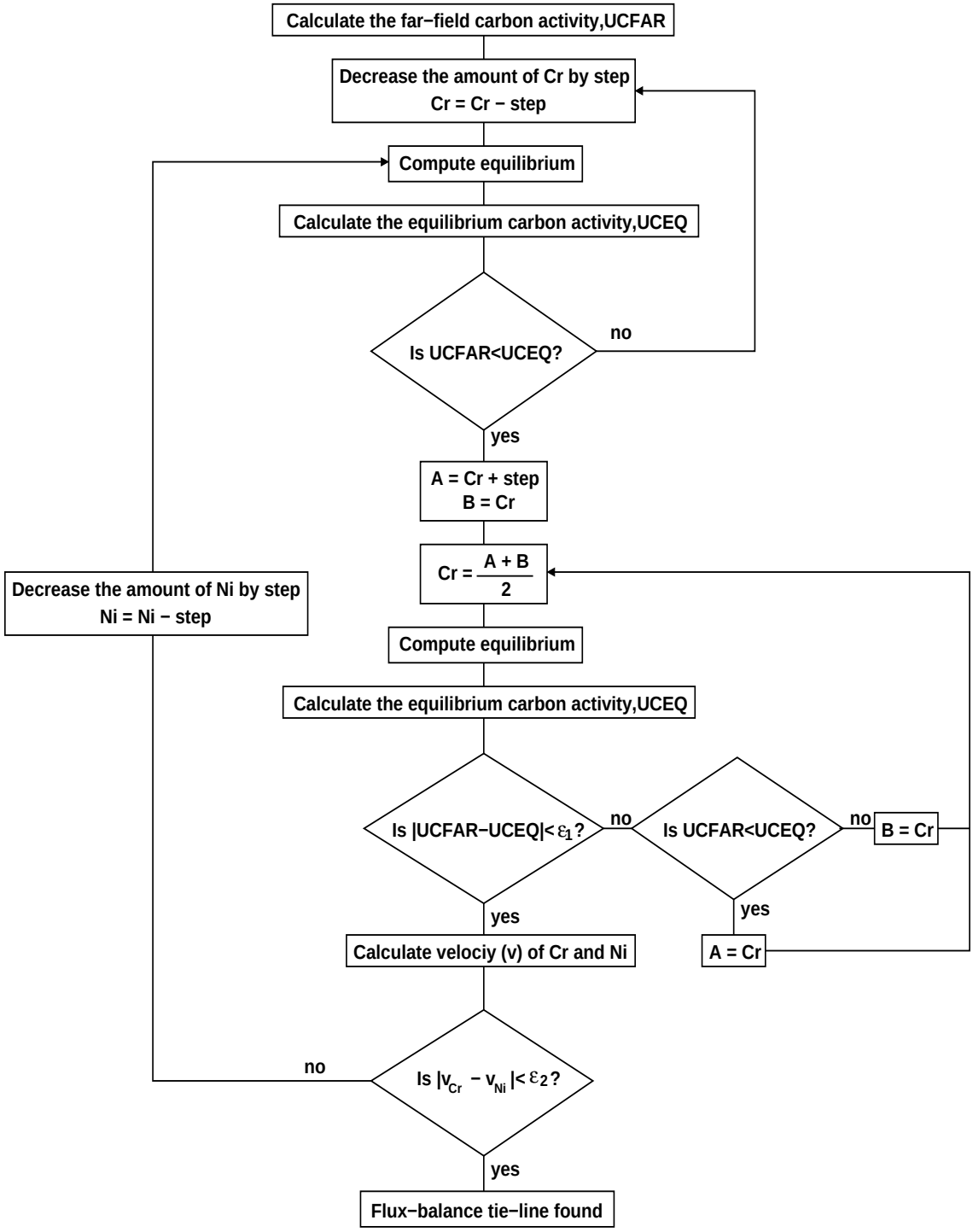

Figure 3.2: The algorithm for finding flux–balance tie–line in a multicomponent system. The step is set to $\frac{1}{50}$ of the initial composition of each element. ε_1 and ε_2 are the control limits.

3.4 Diffusion Equation

After determining the flux–balance tie–line, the concentration profile can be predicted based on a diffusion equation. Consider the flux of element i in the

lattice–fixed f.o.r.:

$$J_i^L = -c_i M_i \nabla \mu_i = -c_i M_i \sum_{k=1}^{n-1} \frac{\partial \mu_i}{\partial x_k} \nabla x_k \tag{3.12}$$

where c_i is the concentration of element i and M_i is mobility of element i. The diffusion equation for the lattice–fixed f.o.r. in a multicomponent system is given as:

$$\frac{\partial c_i}{\partial t} = -\nabla \cdot J_i^L \tag{3.13}$$

The frame of reference in this model is taken as the volume–fixed f.o.r to account for the Kirkendall effect in multicomponent systems [37]. It is defined as no net flow of volume:

$$\sum_i V_i^p J_i^V = 0 \tag{3.14}$$

where V_i^p is the partial molar volume of element i and J_i^V is the flux of element i in the volume–fixed f.o.r.

The relationship between fluxes of the lattice–fixed f.o.r. and the volume–fixed f.o.r. can be written as:

$$J_i^V = J_i^L + c_i v \tag{3.15}$$

where v is the velocity of the lattice–fixed f.o.r. in the volume–fixed f.o.r. This leads to:

$$J_i^V = -\sum_k \left(\delta_{ik} - c_i V_k^p\right) J_k^L \tag{3.16}$$

$$J_i^V = -\sum_k \left(\delta_{ik} - c_i V_k^p\right) c_k M_k \nabla \mu_k \tag{3.17}$$

Equation 3.17 can be rewritten as [38]:

$$J_i^V = -\sum_k A_{ik} \nabla \mu_k \tag{3.18}$$

where $A_{ik} = \left(\delta_{ik} - c_i V_k^p\right) c_k M_k$. The diffusion equation based on Fick's 2$^{\text{nd}}$ law is thus expressed as:

$$\frac{\partial c_i}{\partial t} = -\nabla \cdot J_i^V \tag{3.19}$$

$$\frac{\partial c_i}{\partial t} = -\nabla \sum_{k=1}^{n} A_{ik} \nabla \mu_k \tag{3.20}$$

3.5 Finite Difference Method

In this work, finite difference method is used to solve the diffusion Equation 3.20, in a set of grid points with equal spacing as shown in Figure 3.3. A FORTRAN program has been written based on the finite difference method to solve the diffusion equation. This program is allowed to interface with a thermodynamic software, MTDATA to work directly with the chemical potential gradient.

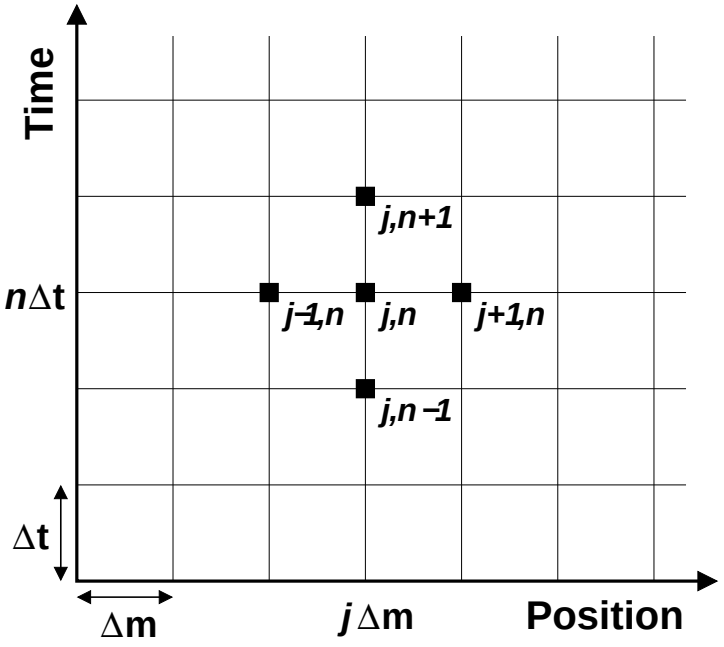

Figure 3.3: Diagram showing a set of equally spaced grid points in a finite difference method where j is the node, Δm is the spacing, Δt is the time step and n is the number of the time step. After [39].

In a finite difference method, it is common to use a forward difference approximation for the time derivative and a central difference approximation for the spatial derivative. For a function Y and its derivatives are single–valued, finite and continuous functions of b, the slope of tangent at Q can be approximated by the slope of the chord QR (Figure 3.4), known as forward difference approximation [39]:

$$Y'(b) = \frac{1}{s}\{Y(b+s) - Y(b)\} \tag{3.21}$$

Alternatively, it can also be approximated with the central difference approximation [39]:

$$Y'(b) = \frac{1}{2s}\{Y(b+s) - Y(b-s)\} \tag{3.22}$$

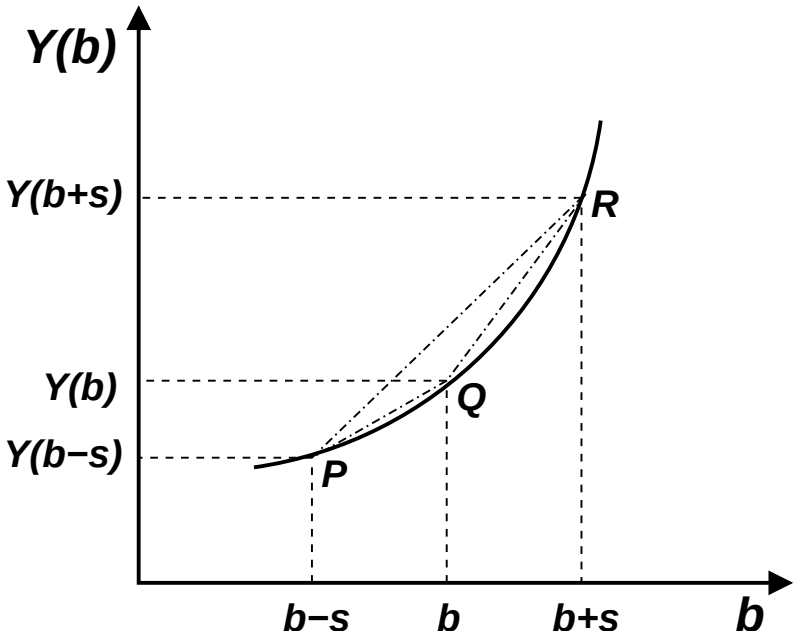

Figure 3.4: Diagram showing forward and central difference approximations. After [39].

In solving the diffusion equation in this model, the forward difference approximation is used for time (Equation 3.23) and the central difference approximation is used for the spatial derivation (Equation 3.24) which leads to Equation 3.25 [38]:

$$\frac{\partial c_i}{\partial t} = \frac{c_i^{j,n+1} - c_i^{j,n}}{\Delta t} \tag{3.23}$$

$$-\nabla \sum_{k=1}^{n} A_{ik} \nabla \mu_k = \frac{1}{(\Delta m)^2} \sum_k \left[A_{ik}^{j+\frac{1}{2},n} \left(\mu_k^{j+1,n} - \mu_k^{j,n} \right) - A_{ik}^{j-\frac{1}{2},n} \left(\mu_k^{j,n} - \mu_k^{j-1,n} \right) \right] \tag{3.24}$$

$$\frac{c_i^{j,n+1} - c_i^{j,n}}{\Delta t} = \frac{1}{(\Delta m)^2} \sum_k \left[A_{ik}^{j+\frac{1}{2},n} \left(\mu_k^{j+1,n} - \mu_k^{j,n} \right) - A_{ik}^{j-\frac{1}{2},n} \left(\mu_k^{j,n} - \mu_k^{j-1,n} \right) \right] \tag{3.25}$$

Rearrange Equation 3.25:

$$c_i^{j,n+1} = c_i^{j,n} + \frac{\Delta t}{(\Delta m)^2} \sum_k \left[A_{ik}^{j+\frac{1}{2},n} \left(\mu_k^{j+1,n} - \mu_k^{j,n} \right) - A_{ik}^{j-\frac{1}{2},n} \left(\mu_k^{j,n} - \mu_k^{j-1,n} \right) \right] \tag{3.26}$$

where $A_{ik}^{j+\frac{1}{2},n}$ and $A_{ik}^{j-\frac{1}{2},n}$ are defined as:

$$A_{ik}^{j+\frac{1}{2},n} = \frac{1}{2}\left[A_{ik}^{j,n} + A_{ik}^{j+1,n}\right] \tag{3.27}$$

$$A_{ik}^{j-\frac{1}{2},n} = \frac{1}{2}\left[A_{ik}^{j,n} + A_{ik}^{j-1,n}\right] \tag{3.28}$$

Although this finite difference method is computationally simple, it is only stable for values of Δt verifying $D\frac{\Delta t}{(\Delta m)^2} \leq \frac{1}{2}$ [40]. Qualitatively, this means the diffusion length during one time step must be less than the space interval. It is better to have smaller values of Δt in order to obtain high numerical accuracy in a finite difference method. However, this will take longer computation time.

3.6 Summary

A model which is interfaced with MTDATA was developed to deal with grain boundary precipitation in austenitic stainless steels. This model takes proper account of the multicomponent effects. In addition, the diffusion profile is predicted based on the chemical potential gradient rather than the conventional concentration gradient. The tie–line is determined by balancing the fluxes of all elements with isoactivity of carbon. A numerical approach – finite difference method is applied to solve the diffusion equation simultaneously for all elements.

Chapter 4

Results and Discussion

A model has been developed in this work to express sensitisation in austenitic stainless steels. FORTRAN programs were written which interfaced with MTDATA to predict the chromium concentration profile in the vicinity of the grain boundary. The results obtained are compared against data in the published literature.

4.1 Interface Chromium Concentration

As mentioned in the previous chapter, an assumption is made that the carbon activity at the carbide–matrix interface is almost equal to the far–field carbon activity as the mobility of carbon is very large relative to substitutional elements. Thus, an isoactivity tie–line in a multicomponent system first has to be determined. Once the isoactivity tie–line is found, the chromium concentration in the matrix at the carbide–matrix interface ($c_{Cr}^{\gamma\beta}$) can be determined.

In order to compare with previous models, predictions of $c_{Cr}^{\gamma\beta}$ have been made based on the composition of type 304 austenitic stainless steels as given in Table 4.1. Only the formation of $M_{23}C_6$ carbide is modelled in the present work.

	Composition / wt%			
AISI type	**Fe**	**Cr**	**Ni**	**C**
304	72.71	18.48	8.75	0.06

Table 4.1: Composition of type 304 austenitic stainless steel [41].

Figure 4.1 compares the calculated $c_{Cr}^{\gamma\beta}$ as a function of temperature, against previous work. The measured data shown in the figure were obtained by Bruemmer *et al.* [41] using the scanning transmission electron microscope with an energy dispersive X–ray spectrometer (STEM–EDS). Only measurements at a region about 25 nm from the grain boundary were able to be taken due to the beam broadening effect when the incident beam passes through the specimen, as shown in Figure 4.2. Measurements of $c_{Cr}^{\gamma\beta}$ obtained using such analytical techniques are usually overestimated since it is difficult to localise the analysis to the matrix (γ) at the interface.

Predicted values should therefore be less than those measured.

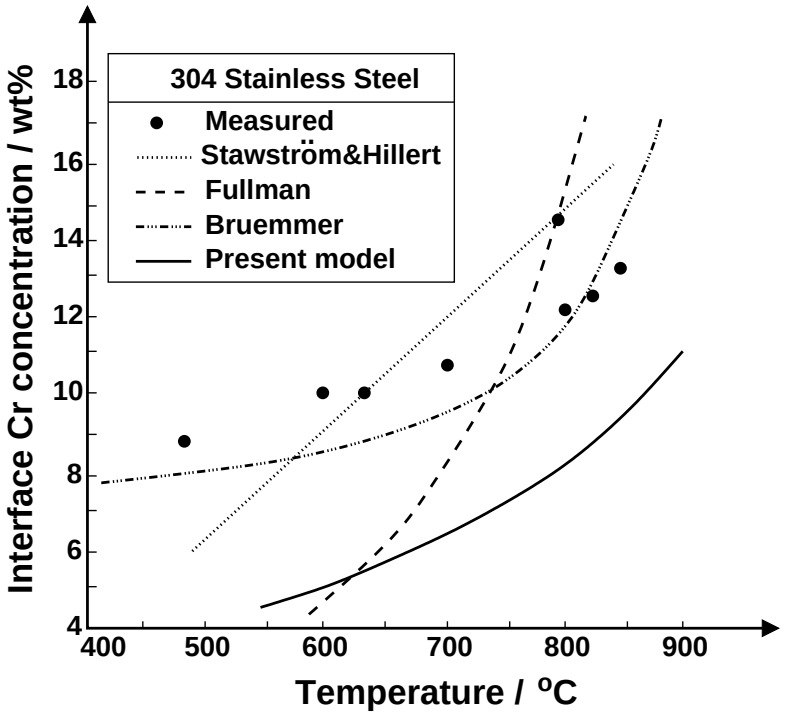

Figure 4.1: Comparison of measured and predicted $c_{Cr}^{\gamma\beta}$ values.

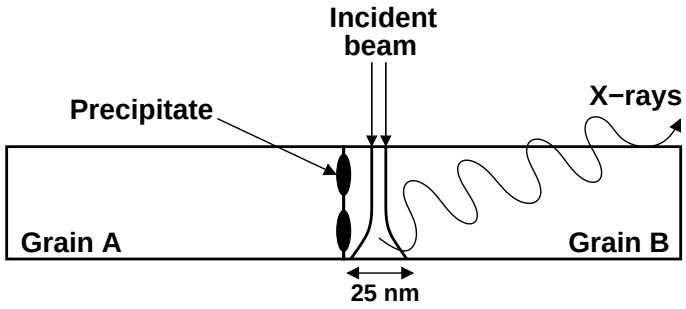

Figure 4.2: Schematic drawing of beam broadening effect. After [42].

Earlier approaches by Stawström and Hillert [8], and Fullman [20] overpredicted $c_{Cr}^{\gamma\beta}$ at high temperatures. Bruemmer [9] applied an empirical relation which was obtained by direct measurements of chromium–depletion. It is not therefore surprising that Bruemmer's model is in good agreement with the measured data.

The present predictions are consistently lower than the measured data, as shown in Figure 4.1. This appears to be correct as the measured data should be higher due to the technique limitations mentioned before. This point will be discussed further later in the thesis. The predicted results also follow the trend of experimental data in which $c_{Cr}^{\gamma\beta}$ increases with temperature.

4.2 Concentration Profile versus Distance

Simulations were conducted using the present model to predict the time progression of the concentration profile from the carbide–matrix (β/γ) interface into the matrix (γ), for all the elements involved. By considering diffusion through an unit surface area, the volume of material considered in the calculations is given by :

$$V = z' \times A \tag{4.1}$$

where z' is the maximum distance from the β/γ interface and A is the unit surface area. Figure 4.3 shows the effect of material volume on the chromium concentration profile. It can be seen that the concentration profile is sensitive to V at small volumes. However, it eventually becomes ceases to be so at large volumes. Thus, all the subsequent predictions were made based on a fixed volume of material, 10×10^{-6} m^3. Even larger volumes can be selected but the computing times become prohibitive with little gain in accuracy.

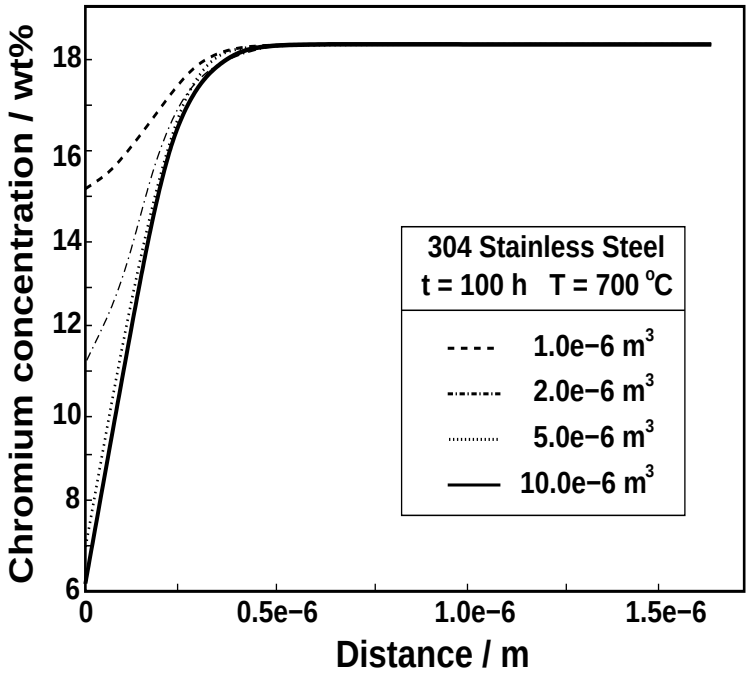

Figure 4.3: Effect of volume of material on the concentration profile.

In order to compare with published literature, the composition of the alloys used for the simulations are given in Table 4.2. Typical concentration profiles for iron, chromium and nickel are shown in Figure 4.4. The origin point of these profiles will change as time increases. This will be discussed in more detail later. The diffusion profile of interstitial carbon is not calculated explicitly in the present model as an even carbon activity is assumed in the whole material. The distance used in the following figures refers to that from the β/γ interface into the γ.

AISI type	Composition / wt%			
	Fe	Cr	Ni	C
304	72.710	18.48	8.75	0.060
316LN–1	73.942	16.25	9.78	0.028
316LN–3	73.844	16.32	9.81	0.026

Table 4.2: Compositions of type 304, 316LN–1 and 316LN–3 austenitic stainless steels used for simulations in the present work [5, 41].

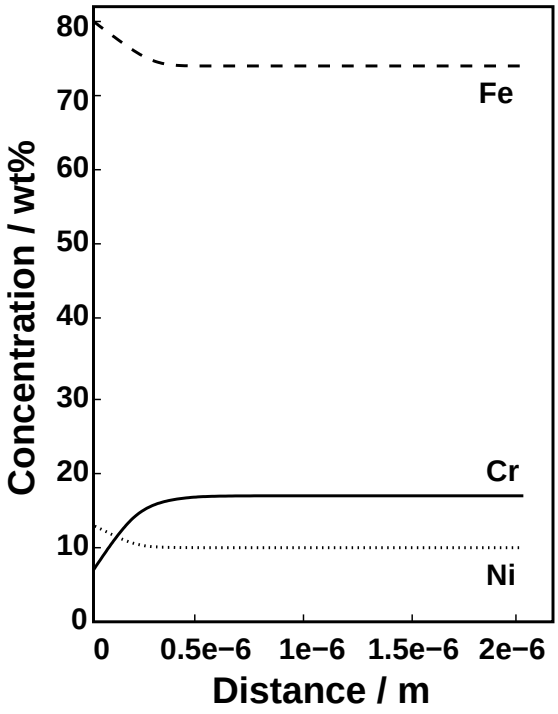

Figure 4.4: Typical concentration profiles of iron, chromium and nickel for 316LN–3 stainless steel at 700 °C after 100 h.

4.2.1 Width of Depleted–Zone

The $c_{Cr}^{\gamma\beta}$ value and the width of chromium–depleted zone varies with heat treatment temperature and time. As shown in Figure 4.5(a), the $c_{Cr}^{\gamma\beta}$ rises as time progresses. The width of the depleted zone also increases with time, leading to a flatter chromium profile near the grain boundaries.

When the carbide precipitate grows, the carbon content in the matrix decreases, causing a decrease in the carbon activity. The chromium activity at the carbide–matrix interface thus increases and leads to an increase in $c_{Cr}^{\gamma\beta}$. The width of the depleted zone also increases with time and a flatter profile is obtained. The corresponding volume fraction of $M_{23}C_6$ cabide is also plotted in Figure 4.5(b). It is shown that the rate of carbide formation reduces with time as carbon is depleted from the matrix.

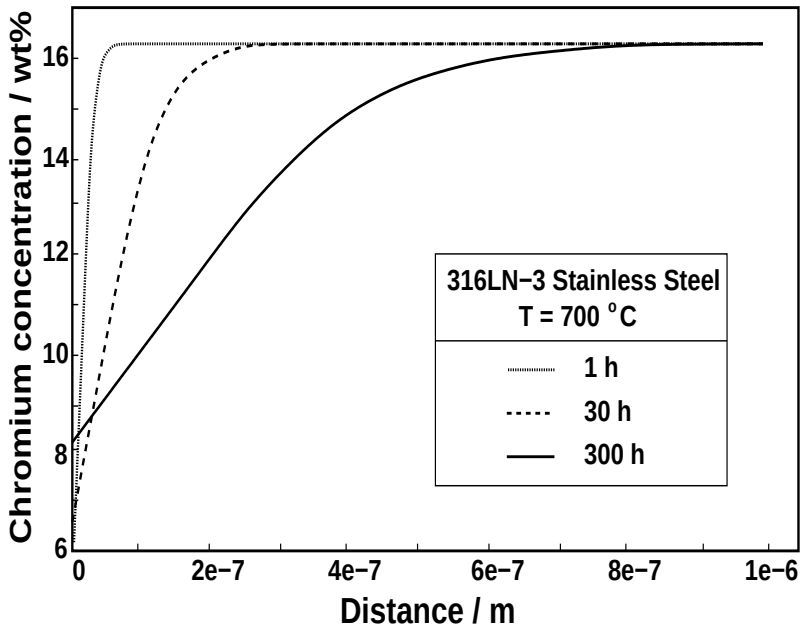

(a)

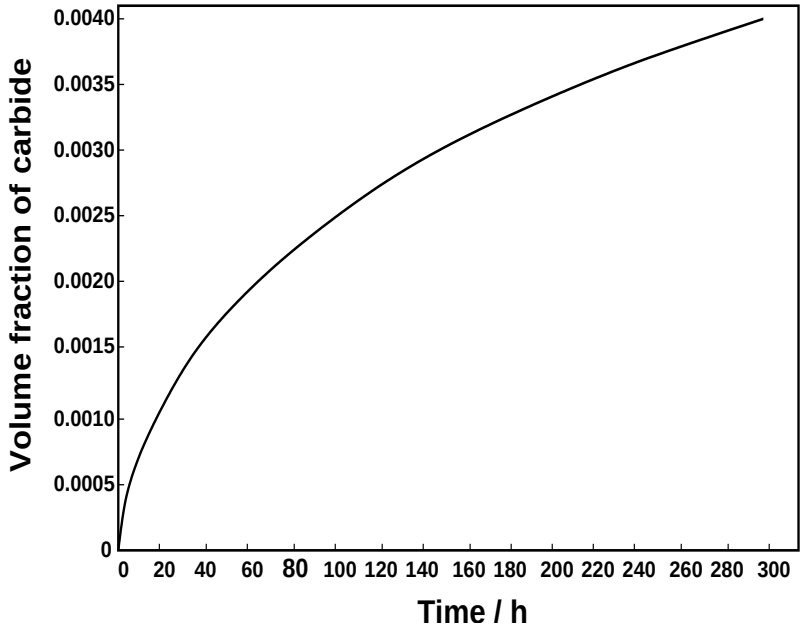

(b)

Figure 4.5: (a) Chromium concentration profile of type 316LN–3 stainless steel at 700 °C after 1 h, 30 h and 300 h with the $c_{Cr}^{\gamma\beta}$ values of 6.11 wt%, 6.45 wt% and 8.32 wt% respectively. (b) The corresponding carbide volume fraction plot.

4.2.2 Heat Treatment Temperature

The heat treatment temperature has significant effects on the chromium concentration profile. Figure 4.6(a) shows the change in the shape of the profile as a

function of temperature after 50 h for type 304 stainless steel. It is clearly seen that $c_{Cr}^{\gamma\beta}$ and the width of the depleted zone increases with increasing temperature for a given treatment time. It is also clear from the corresponding carbide volume fraction plots (Figure 4.6(b)) that the rate of carbide formation increases when temperature rises.

The equilibrium fraction of the FCC_A1 and $M_{23}C_6$ phases and its composition for type 304 stainless steel are separately calculated using MTDATA, in Table 4.3. As can be seen from the table, the equilibrium mole fraction of $M_{23}C_6$ decreases with increasing temperature. Figure 4.6(b) shows that equilibrium is achieved more rapidly at high temperature compared with low temperature.

Temperature / °C	**Phase**	**Composition / wt%**				**Mole fraction**
		Fe	**Cr**	**Ni**	**C**	
600	FCC_A1	73.38	17.78	8.84	0.00086	0.9869
	$M_{23}C_6$	9.16	85.19	0.00083	5.65	0.0131
700	FCC_A1	73.31	17.85	8.84	0.00456	0.9877
	$M_{23}C_6$	12.54	81.83	0.00089	5.63	0.0123
800	FCC_A1	73.15	18.02	8.82	0.01687	0.9904
	$M_{23}C_6$	16.18	78.20	0.00090	5.62	0.0096

Table 4.3: Equilibrium fraction of FCC_A1 and $M_{23}C_6$ phases and its composition as a function of temperature for type 304 stainless steel.

Simulations were also conducted for low carbon austenitic stainless steel (type 304L) which is developed for reduced sensitisation. The composition for type 304L stainless steel used in the simulations are given in Table 4.4.

AISI type	**Composition / wt%**			
	Fe	**Cr**	**Ni**	**C**
304L	72.74	18.48	8.75	0.03

Table 4.4: Composition of type 304L austenitic stainless steel.

Figure 4.7(a) shows the chromium concentration profiles for type 304L stainless steel at different temperatures after 50 h. It is seen that $c_{Cr}^{\gamma\beta}$ achieves a higher value in low carbon type 304L stainless steel compared with 304 stainless steel (Figure 4.6(a)) after the same treatment time. This means that the self–healing process begins earlier in a low carbon alloy, leading to a higher value of $c_{Cr}^{\gamma\beta}$ for a given treatment time. This effect is shown clearly at higher temperature, 800 °C.

The equilibrium mole fraction of $M_{23}C_6$ for 304L is much lower compared with 304 stainless steel, as can be seen in Table 4.5. It follows that the likelihood for sensitisation to occur in low carbon stainless steel is reduced.

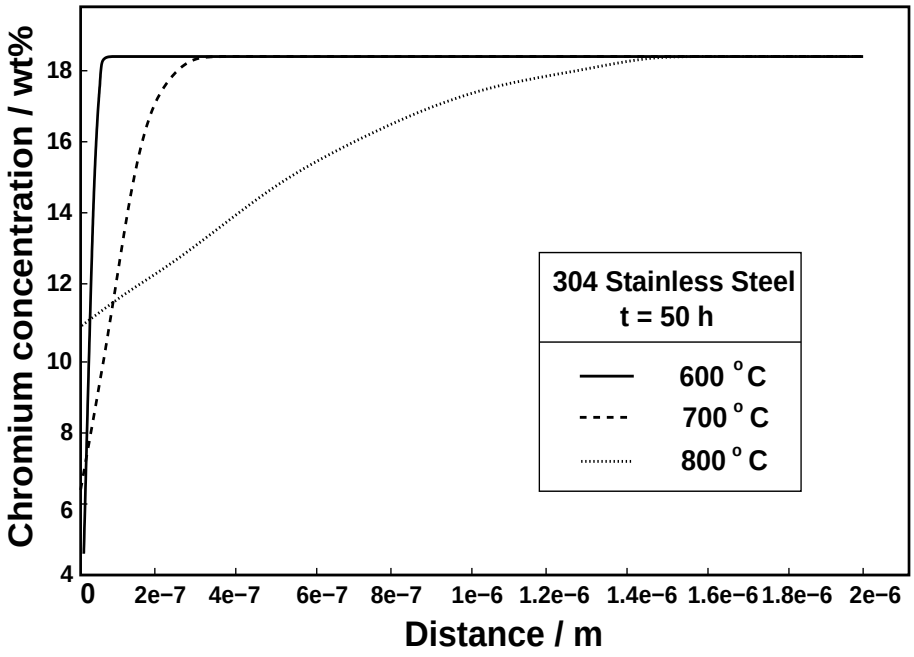

(a)

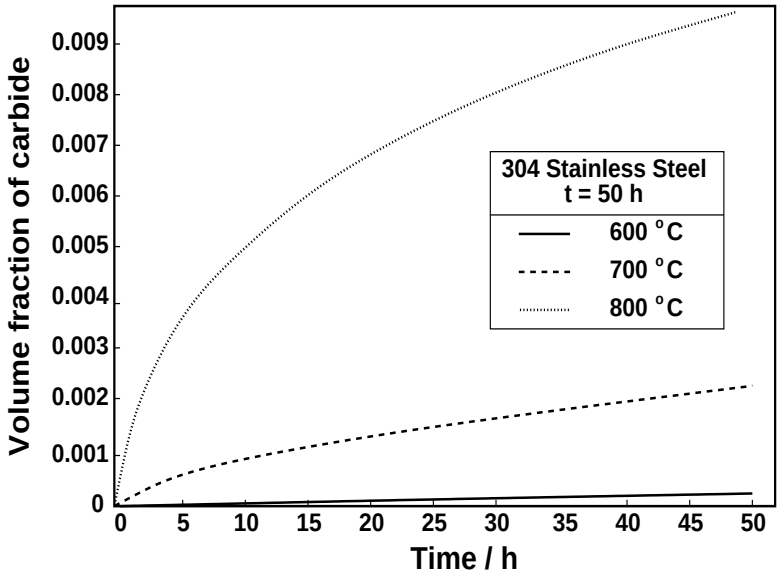

(b)

Figure 4.6: (a) Effect of temperature on the chromium concentration profile after heat treatment time 50 h for type 304 stainless steel. The $c_{Cr}^{\gamma\beta}$ values are 4.57 wt%, 6.31 wt% and 11.01 wt% for 600 °C, 700 °C and 800 °C respectively. (b) The corresponding carbide volume fraction plots at different temperatures.

4.3 Concentration versus Time Plot

The chromium concentration versus time, for a number of nodes in the finite difference scheme, is plotted and shown in Figure 4.8. The chromium concentration

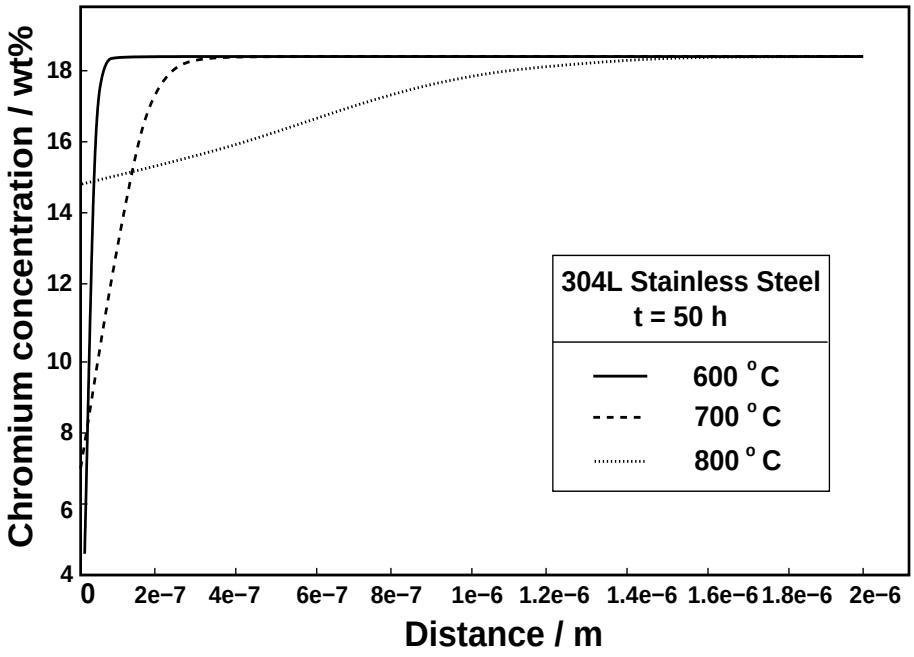

(a)

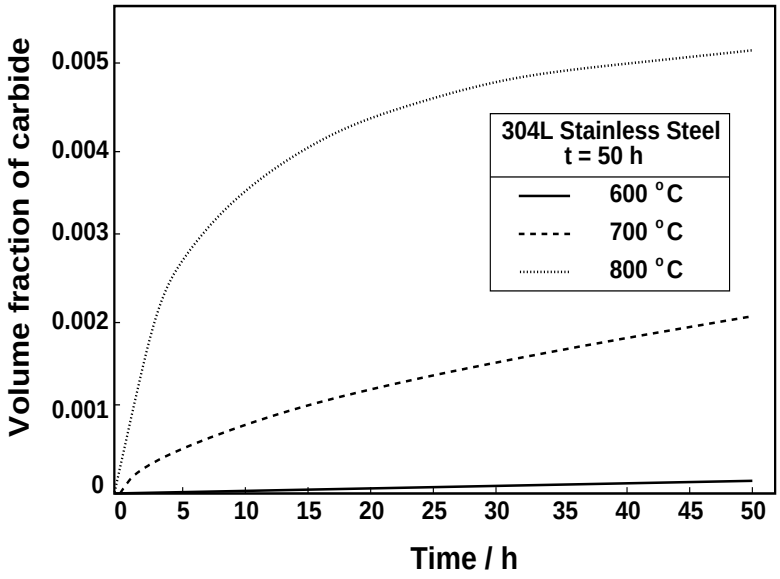

(b)

Figure 4.7: (a) Effect of temperature on the chromium concentration profile after heat treatment time 50 h for type 304L stainless steel. The $c_{Cr}^{\gamma\beta}$ values are 4.68 wt%, 7.08 wt% and 14.78 wt% for 600 °C, 700 °C and 800 °C respectively. (b) The corresponding carbide volume fraction plots at different temperatures.

at the carbide–matrix interface, $c_{Cr}^{\gamma\beta}$, is represented by Node 0. It can be clearly seen that $c_{Cr}^{\gamma\beta}$ increases gradually with time. This correctly predicts desensitisation

Temperature / °C	Phase	Composition / wt%				Mole fraction
		Fe	Cr	Ni	C	
600	FCC_A1	73.07	18.13	8.80	0.00084	0.9935
	$M_{23}C_6$	8.99	85.36	0.00081	5.65	0.0065
700	FCC_A1	73.02	18.19	8.79	0.00447	0.9943
	$M_{23}C_6$	12.32	82.05	0.00087	5.64	0.0057
800	FCC_A1	72.88	18.33	8.77	0.01651	0.9970
	$M_{23}C_6$	15.91	78.46	0.00087	5.62	0.0030

Table 4.5: Equilibrium fraction of FCC_A1 and $M_{23}C_6$ phases and its composition as a function of temperature for type 304L stainless steel.

during prolonged heat treatment time.

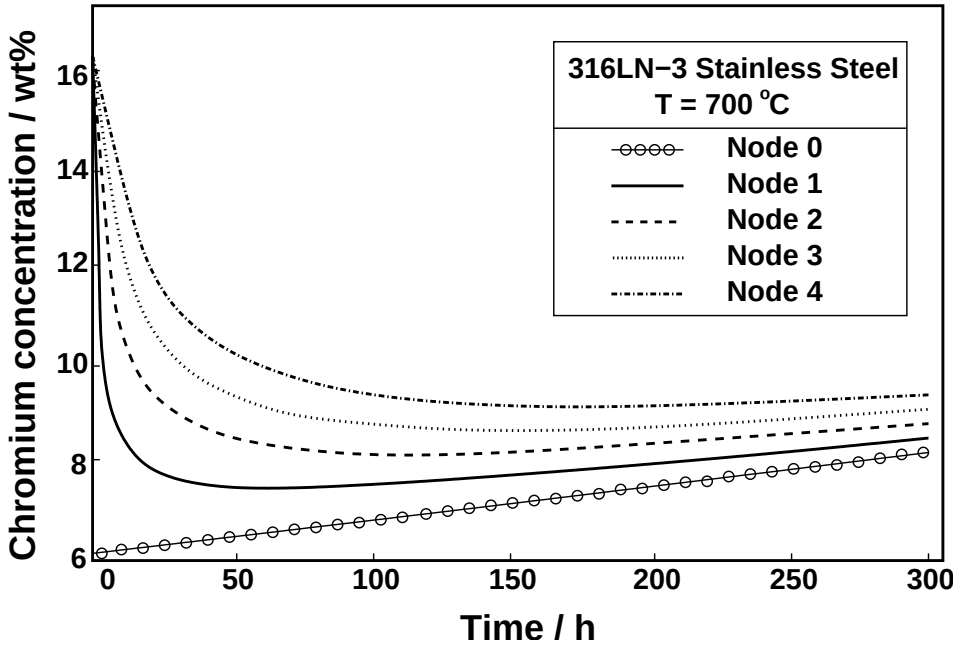

Figure 4.8: Chromium concentration profile versus time for type 316LN–3 stainless steels at 700 °C for treatment time 300 h. The spacing between each node is ≈14 nm.

The concentration versus time plot (Figure 4.8) shows that the present model exhibits the correct behaviour of carbide precipitation from Node 1 onwards. As can be seen from the curves (Node 1 to Node 4), the chromium concentration decreases gradually with time, showing the depletion of chromium towards the γ/β interface during carbide precipitation until reaching a minimal value which corresponds to a partial thermodynamic equilibrium between the carbide and matrix. When self–healing begins, the chromium concentration slowly rises with increasing time, approaching equilibrium. The spacing between each node is ≈14 nm.

4.4 Comparison with Further Literature Data

Comparisons are made with some published literature data to validate the chromium concentration profiles predicted by the present model. As emphasised in the earlier section, due to technique limitations, it is not easy to obtain experimental data exactly at the grain boundary. The measured data were obtained at ≈25 nm from the grain boundary [41]. Thus, it is best to compare the predictions at a distance of ≈25 nm from the grain boundary with those measured data, as shown in Figure 4.9. It appears that the predictions made with the present model are in good agreement with the measured data, giving a linear relationship between the measured and predicted data at ≈25 nm.

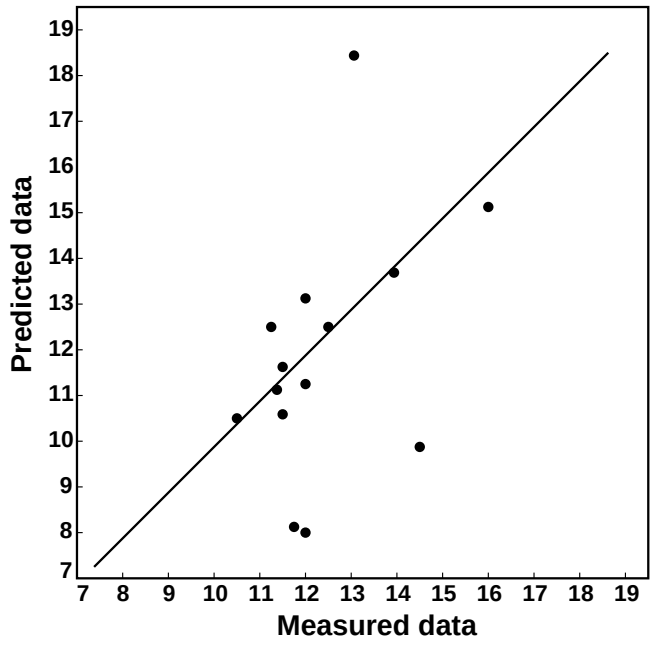

Figure 4.9: Comparison of measured and predicted chromium concentration at distance ≈25 nm.

Figure 4.10 shows a comparison between the predicted chromium profile and the measured data by Bruemmer [41]. It is evident that the predictions are in good agreement with those data measured at a small distance away from the grain boundary. This further proves the ability of the present model in predicting chromium concentration profile at the grain boundary region. The comparison also gives confidence in the ability of the model to predict $c_{Cr}^{\gamma\beta}$.

More comparisons are made on the predictions by the present model with Hall and Briant's data. Experiments were conducted by Hall and Briant to obtain the measured data. It is shown in Figure 4.11 that the predictions with the present model are in good agreement with those data measured at a small distance away from the grain boundary. The values of $c_{Cr}^{\gamma\beta}$ are, as expected, lower than the measured data. This appears to be correct for the reasons described earlier.

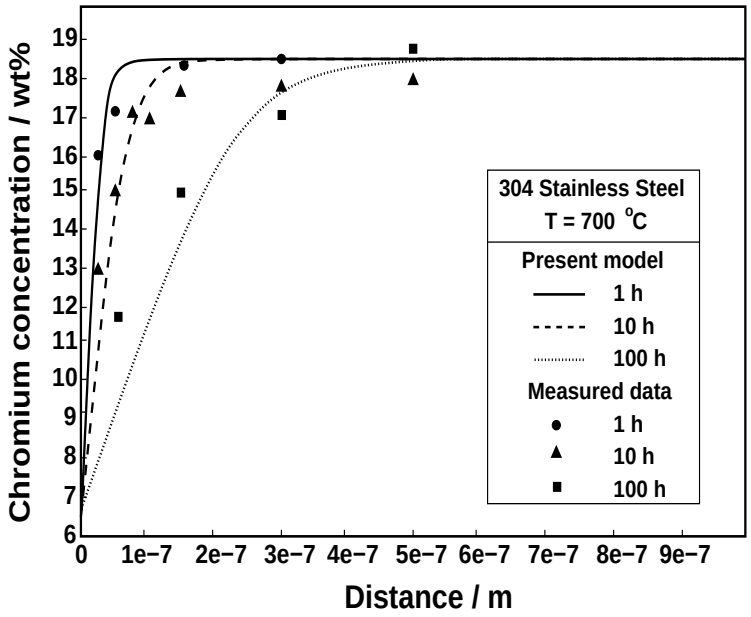

(a)

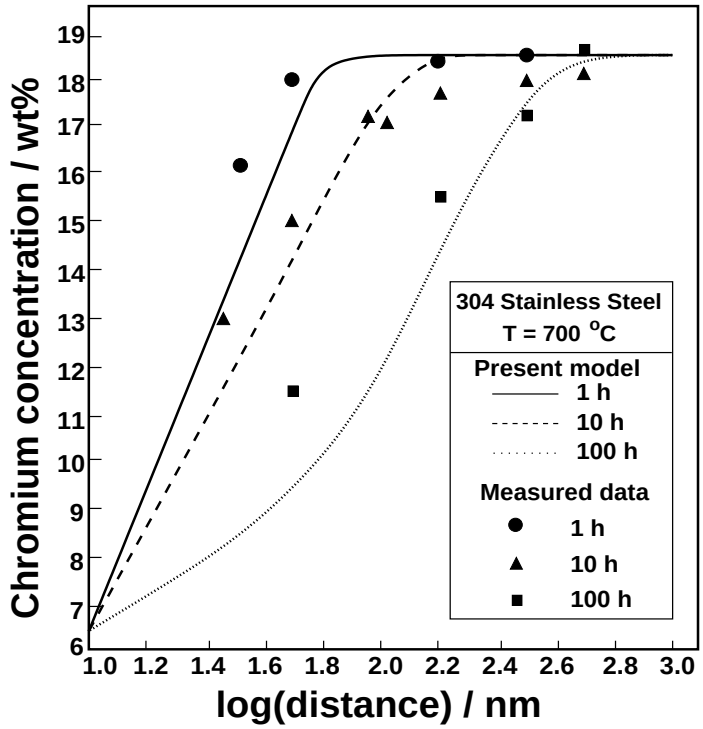

(b)

Figure 4.10: (a) Comparison of predicted chromium concentration profile at the grain boundary region and the measured data by Bruemmer [41]. (b) The same chromium concentration plot versus log distance.

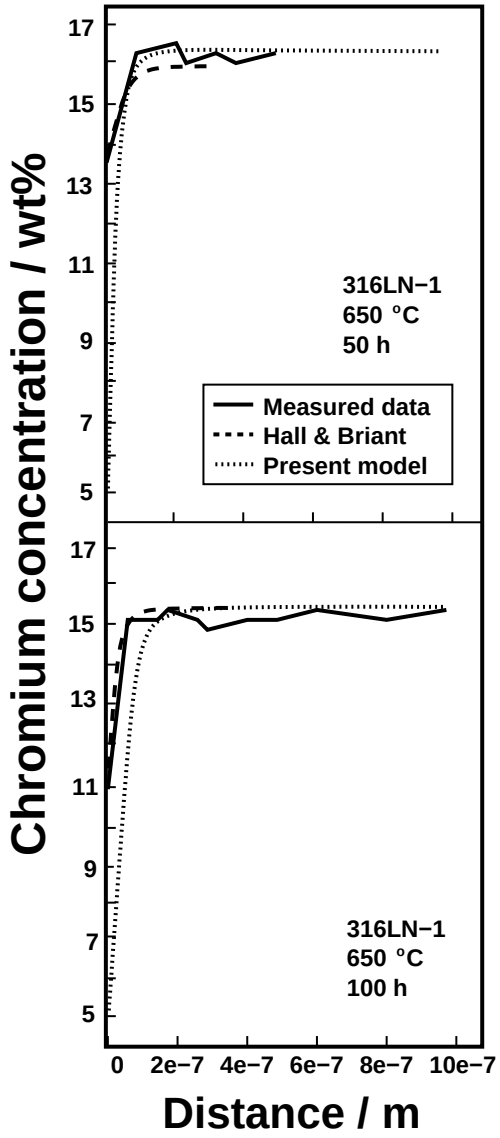

Figure 4.11: Comparison of measured and predicted chromium concentration profile for 316LN–1 stainless steel at 650 °C.

4.5 Summary

A general model to predict sensitisation in austenitic stainless steels has been developed. Precipitation reaction in multicomponent systems has been accounted for by interfacing the model with thermodynamic software, MTDATA. Several simulations were conducted and the results obtained are discussed and compared against the literature data. The predictions are in good agreement with the measured data, proved the ability of the present model in predicting chromium concentration profile at the grain boundary region. It is also shown that the present work manages to predict the minimum chromium concentration at the carbide–matrix interface which is difficult to obtain using experimental technique.

Chapter 5

Summary and Future Work

The wide application of austenitic stainless steels in industry is greatly affected by the sensitisation phenomena at the grain boundary region, leading to deterioration of corrosion resistance in steels. The main aim of this research was to develop a general physical model to predict the likelihood of sensitisation in austenitic stainless steels.

A review has been conducted of previous attempts on modelling grain boundary precipitation. It revealed that work on modelling grain boundary precipitation has in general represented multicomponent effects rather badly. Grain boundary precipitation reactions in austenitic stainless steels are, in practice, complex with significant interactions between solutes.

A general model, which interfaced with a thermodynamic software, MTDATA has been created, which is capable of predicting concentration variations in all types of austenitic stainless steels. Complex thermodynamic calculations can thus be performed without making unnecessary approximations. Most of the previous work applied the mass–balance tie–line method in determining the diffusion profiles for all the elements involved. However, different elements involved in the precipitation reaction often have vastly different diffusivities. Thus, the more appropriately flux–balance tie–line method in which the fluxes of all elements are balanced based on isoactivity of carbon is used in this research.

A finite difference method has been applied to solve the diffusion equations based on chemical potential gradients rather than concentration gradients, thereby accurately predicting the concentration profile of all elements. The effects of multicomponent system are thus properly taken into account in the present model.

Predictions made with this model have been discussed and compared with published literature data. The results obtained are in good agreement with measured data, further proved the ability of the present model in predicting the concentration profiles at the grain boundary region.

Future research can be conducted to improve this work by studying the effects of grain boundary diffusion and grain boundary structure on modelling the precipitation kinetics. It is also worth to take into account the nucleation kinetics, the grain size effects and to study the soft impingement effects on modelling complex diffusion kinetics, further improving the predictability of the present model. It would also be

useful to conduct research on the effects of multicomponent capillarity on modelling grain boundary precipitation.

Appendix

MAP_STEEL_SENSITISATION_AUSTENITIC

This appendix presents the model described in Chapter 3 and associated documentation following the MAP format, http://www.msm.cam.ac.uk/map/mapmain.html.

1 Provenance of Source Code

Chia Hooi Too and Sourmail T.
Phase Transformations and Complex Properties Group,
Department of Materials Science and Metallurgy,
University of Cambridge,
Cambridge, CB2 3QZ,
United Kingdom.

This program is interfaced with MTDATA:
National Physical Laboratory,
Teddington,
Middlesex,
TW11 0LW,
United Kingdom.

Added to MAP: August 2002.

2 Purpose

A program for the prediction of sensitisation of austenitic stainless steels as a function of alloy composition, heat treatment temperature and time.

3 Specification

Language: FORTRAN
Product Form: Source Code
Operating System: tested on Linux.

4 Description

MAP_STEEL_SENSITISATION_AUSTENITIC contains the program which enable the user to predict sensitisation of austenitic stainless steels as a function of chemical composition, temperature and heat treatment time. All thermodynamic calculations are performed internally by MTDATA. The software uses MTDATA *.mpi* database file which has to be created earlier by the user, using the ACCESS module of MTDATA. Once uncompressed, MAP_STEEL_SENSITISATION_AUSTENITIC contains:

sensitisation.f
The source code for the program.
compile
A unix shell script to compile the program and link it to MTDATA object files.
DATA
A file containing information about the name of the component in solvent, the matrix phase, composition filename, database filename and output filename.
DATABASE.mpi
An example database file for the model.
CPTFIL
A file containing information about the composition of the steel and heat treatment temperature.
PROFILE
Contains information about the distance used in the model.
OUTFIL
An example output file for the model.
README
A text file containing instructions for running the program.

5 References

Chia Hooi Too, *Master of Philosophy (M.Phil.) thesis, Chapter 3*, University of Cambridge, 2002.

6 Input parameters

The user is required to provide the alloy chemical composition, heat treatment time and temperature, and the maximum distance from the grain boundary to the matrix.

7 Output parameters

The model will give the concentration of all elements in the system as a function of time and distance. The volume fraction of carbide is also calculated. The output is written in the file OUTFIL.

Keywords
Sensitisation, grain boundary precipitation, austenitic stainless steels.

Bibliography

[1] Lacombe P., Baroux B., and Beranger G., editors. *Stainless Steels.* Les Editions de Physiques, Les Ulis, 1993.

[2] Honeycombe R. W. K. and Bhadeshia H. K. D. H. *Steels–microstructure and properties.* Edward Arnold, 2nd edition, 1995.

[3] Marrow J. http://www.umist.ac.uk/matsci/research/intmic/mterials/britstel/ss_aus/sample.htm, 2001.

[4] Parr J. G. and Hanson A. *An Introduction to Stainless Steel.* American Society For Metals, 1965.

[5] Hall E. L. and Briant C. L. *Metall. Trans. A*, 15A:793–811, 1984.

[6] Shimada M., Kokawa H., Wang Z. J., Sato Y. S., and Karibe I. *Acta Mater.*, 50:2331–2341, 2002.

[7] Gooch T. G. and Willingham D. C. *Weld Decay in Austenitic Stainless Steel.* Welding Institute, Cambridge, United Kingdom, 1975.

[8] Stawström C. and Hillert M. *Journal of The Iron and Steel Institute*, pages 77–85, 1969.

[9] Bruemmer S. M. *Corrosion*, 46:698–709, 1990.

[10] Was G. S. and Kruger R. M. *Acta Metall.*, 33:841–854, 1985.

[11] Mayo W. E. *Mater. Sci. Eng. A*, A232:129–139, 1997.

[12] Sahlaoui H., Sidhom H., and Philibert J. *Acta Mater.*, 50:1383–1392, 2002.

[13] Bhadeshia H. K. D. H. *Progress in Materials Sci.*, 29:322–383, 1985.

[14] Nishizawa T. unpublished work.

[15] Shvartz G. L. and Kristal M. M. *Corrosion of Chemical Apparatus.* Chapman & Hall, London, 1959.

[16] *Corrosion of Metals.* Defense Press, 1955. In Russian.

[17] Bäumel A., Bühler H. −E., Schüller H. −J., Schwaab P., Schwenk W., and Ternes H. *Corr. Sci.*, 4:89–103, 1964.

[18] Bendure R. J., Ikenberry L. C., and Wasweiler J. H. *Trans. AIME*, 221:1032–1039, 1961.

[19] Kohler F. *Chemie*, 91:738, 1960.

[20] Fullman R. L. *Acta Metall.*, 30:1407–1415, 1982.

[21] Hall E. L. and Briant C. L. *Metall. Trans. A*, 16A:1225, 1984.

[22] Briant C. L., O'Toole C. S., and Hall E. L. *Corrosion*, 42:15, 1986.

[23] Was G. S., Tischner H. H., and Latanision R. M. *Metall. Trans. A*, 12A:1397, 1981.

[24] Ballinger R. and Hwang I. EPRI Workshop, 1987.

[25] Kai J. J., Yu G., Tsai C. H., Liu M. N., and Yao S. C. *Metall. Trans. A*, 20A:2057–2067, 1989.

[26] MTDATA. National Physical Laboratory, Teddington, Middlesex, U.K., 1989.

[27] Saunders N. and Miodownik A. P. *CALPHAD – Calculation of Phase Diagrams, A Comprehensive Guide.* Pergamon Press, Oxford, 1998.

[28] Christian J. W. *The Theory of Transformations in Metals and Alloys.* Pergamon Press, Oxford, 1965.

[29] Andersson J.-O. and Ågren J. *J. Appl. Phys.*, 72:1350–1355, 1992.

[30] Ågren J. *J.I.S.I.*, 32:291–296, 1992.

[31] Åkermark T. *Div. of Phys. Metall.*, 44:S–100, 1991.

[32] Jönsson B. *Z. Metallkd.*, 85:502–509, 1994.

[33] Coates D. E. *Metall. Trans.*, 3:1203–1212, 1972.

[34] Coates D. E. *Metall. Trans.*, 4:1077–1086, 1973.

[35] Fujita N. and Bhadeshia H. K. D. H. *Mater. Sci. Techn.*, 15:627–634, 1999.

[36] Sourmail T. *Simultaneous Precipitation Reactions in Creep–Resistant Austenitic Stainless Steels.* PhD thesis, University of Cambridge, 2002.

[37] Kirkaldy J. S. and Young D. J. *Diffusion in the Condensed State.* Institute of Metals, London, 1987.

[38] Sourmail T. and Bhadeshia H. K. D. H. unpublished work. 2002.

[39] Smith G. D. *Numerical Solution of Partial Differential Equations–Finite Difference Methods*. Clarendon Press, Oxford, 2nd edition, 1978.

[40] Mitchell A. R. and Griffiths D. F. *The Finite Difference Method in Partial Differential Equations*. John Wiley & Sons Ltd., 1987.

[41] Bruemmer S. M. and Charlot L. A. *Scripta Metall.*, 20:1019–1024, 1986.

[42] Busby J. T., Allen T. R., Kenik E. A., Zaluzec N. J., and Was G. S. http://tpm.amc.aml.gov/mmc/pubs/mm97/mm97.html, 1997.